2005-09

Analysis of high-resolution COAMPS with observed METOC data to demonstrate atmospheric impact on EM propagation

Murphy, Richard M.

Monterey, California. Naval Postgraduate School

NAVAL POSTGRADUATE SCHOOL

MONTEREY, CALIFORNIA

THESIS

ANALYSIS OF HIGH-RESOLUTION COAMPS™ WITH OBSERVED METOC DATA TO DEMONSTRATE ATMOSPHERIC IMPACT ON EM PROPAGATION

by

Richard M. Murphy

September 2005

Thesis Advisor: K. L. Davidson
Second Reader: Paul Frederickson

Approved for public release; distribution is unlimited.

THIS PAGE INTENTIONALLY LEFT BLANK

REPORT DOCUMENTATION PAGE			Form Approved OMB No. 0704-0188
Public reporting burden for this collection of information is estimated to average 1 hour per response, including the time for reviewing instruction, searching existing data sources, gathering and maintaining the data needed, and completing and reviewing the collection of information. Send comments regarding this burden estimate or any other aspect of this collection of information, including suggestions for reducing this burden, to Washington headquarters Services, Directorate for Information Operations and Reports, 1215 Jefferson Davis Highway, Suite 1204, Arlington, VA 22202-4302, and to the Office of Management and Budget, Paperwork Reduction Project (0704-0188) Washington DC 20503.			
1. AGENCY USE ONLY *(Leave blank)*	**2. REPORT DATE** September 2005	**3. REPORT TYPE AND DATES COVERED** Master's Thesis	
4. TITLE AND SUBTITLE: Title (Mix case letters) Analysis of High-Resolution COAMPS with Observed METOC Data to Demonstrate Atmospheric Impact on EM Propagation			**5. FUNDING NUMBERS**
6. AUTHOR(S) Richard M. Murphy			
7. PERFORMING ORGANIZATION NAME(S) AND ADDRESS(ES) Naval Postgraduate School Monterey, CA 93943-5000			**8. PERFORMING ORGANIZATION REPORT NUMBER**
9. SPONSORING /MONITORING AGENCY NAME(S) AND ADDRESS(ES) N/A			**10. SPONSORING/MONITORING AGENCY REPORT NUMBER**
11. SUPPLEMENTARY NOTES The views expressed in this thesis are those of the author and do not reflect the official policy or position of the Department of Defense or the U.S. Government.			
12a. DISTRIBUTION / AVAILABILITY STATEMENT Approved for public release; distribution is unlimited			**12b. DISTRIBUTION CODE**

13. ABSTRACT (maximum 200 words) Current U.S. Navy Special Warfare and submarine concepts of operations (CONOPS) dictate that *in-situ* environmental data collection is limited or not possible. Therefore, predicted data from operational models, such as the Coupled Ocean Atmosphere Mesoscale Prediction System (COAMPS), are essential to estimate the impacts of environmental conditions on the detection of enemy targets and counter-detection by radar and optical sensors. This study compares the use of high-resolution COAMPS data and *in-situ* shipboard and rawinsonde measurements for detection prediction purposes. The evaluation is based on data from Fleet Exercise SILENT HAMMER conducted off the Southern California coast near San Clemente Island in October 2004. An instrumented vessel was used for continuous surface layer data collection and frequent rawinsonde launches. COAMPS meteorological predictions were obtained at 3- and 9-km resolutions. The shipboard and COAMPS data provided refractivity profiles that were then used with propagation models within the *BUILDER* and AREPS graphical user interfaces to obtain signal-to-noise and propagation loss versus range diagrams. An increase in the horizontal resolution of COAMPS from 9 to 3 km did not significantly improve the prediction of meteorological variables within the lower marine boundary layer. However, counter-intuitively, the higher resolution did slightly improve detection range estimates.

14. SUBJECT TERMS COAMPS, EM propagation, boundary layer, refractivity, AREPS, *Builder*			**15. NUMBER OF PAGES** 94
			16. PRICE CODE
17. SECURITY CLASSIFICATION OF REPORT Unclassified	**18. SECURITY CLASSIFICATION OF THIS PAGE** Unclassified	**19. SECURITY CLASSIFICATION OF ABSTRACT** Unclassified	**20. LIMITATION OF ABSTRACT** UL

NSN 7540-01-280-5500 Standard Form 298 (Rev. 2-89)
Prescribed by ANSI Std. 239-18

THIS PAGE INTENTIONALLY LEFT BLANK

ANALYSIS OF HIGH-RESOLUTION COAMPS™ WITH OBSERVED METOC DATA TO DEMONSTRATE ATMOSPHERIC IMPACT ON EM PROPAGATION

Richard M. Murphy
Lieutenant Commander, United States Navy
B.S., United States Military Academy, 1994

Submitted in partial fulfillment of the
requirements for the degree of

MASTER OF SCIENCE IN METEOROLOGY AND PHYSICAL OCEANOGRAPHY

from the

NAVAL POSTGRADUATE SCHOOL
September 2005

Author: Richard M. Murphy

Approved by: Kenneth L. Davidson
Thesis Advisor

Paul Frederickson
Second Reader

Philip A. Durkee
Chairman, Department of Meteorology

THIS PAGE INTENTIONALLY LEFT BLANK

ABSTRACT

Current U.S. Navy Special Warfare and submarine concepts of operations (CONOPS) dictate that *in-situ* environmental data collection is limited or not possible. Therefore, predicted data from operational models, such as the Coupled Ocean Atmosphere Mesoscale Prediction System (COAMPS®), are essential to estimate the impacts of environmental conditions on the detection of enemy targets and counter-detection by radar and optical sensors. This study compares the use of high-resolution COAMPS® data and *in-situ* shipboard and rawinsonde measurements for detection prediction purposes. The evaluation is based on data from Fleet Exercise SILENT HAMMER conducted off the Southern California coast near San Clemente Island in October 2004. An instrumented vessel was used for continuous surface layer data collection and frequent rawinsonde launches. COAMPS® meteorological predictions were obtained at 3- and 9-km resolutions. The shipboard and COAMPS® data provided refractivity profiles that were then used with propagation models within the *Builder* and AREPS graphical user interfaces to obtain signal-to-noise and propagation loss versus range diagrams. An increase in the horizontal resolution of COAMPS® from 9- to 3-km did not significantly improve the prediction of meteorological variables within the lower marine boundary layer. However, counter-intuitively, the higher resolution did slightly improve detection range estimates.

THIS PAGE INTENTIONALLY LEFT BLANK

TABLE OF CONTENTS

LIST OF FIGURES

LIST OF TABLES

THIS PAGE INTENTIONALLY LEFT BLANK

ACKNOWLEDGMENTS

I'd like to start with thanking Mr. Lee Eddington of the Naval Air Warfare Center, San Diego. His 3-km COAMPS® data was the starting point for this research. Dr. A. Goroch, of the Naval Research Laboratory Monterey, was also instrumental in his assistance with *Builder* software support.

In addition, Professor's Wendell Nuss and Robert Creasey, both of the Department of Meteorology at the Naval Postgraduate School, were terrific with a large portion of their spare time given in helping with data collection and processing. Mr. Kostas Rados, an Associate Professor in the Pollution Control Technologies Department of the Higher Technical Education Institute of Western Macedonia, was also very helpful with the use of his UNIX script file for reading the 3-km COAMPS® data.

This thesis was completed with support from the NPS Maritime Domain Protection Research Group (formerly known as the Maritime Domain Protection Task Force) of the Meyer Institute of Systems Engineering at the Naval Postgraduate School, and from the NETWARCOM funded NPS Trident Warrior/Silent Hammer Analysis TEAM.

THIS PAGE INTENTIONALLY LEFT BLANK

I. INTRODUCTION

A. MOTIVATION

It is imperative to U.S. Naval forces to obtain accurate information, whether from human intelligence or satellite imagery. Taking the knowledge gained one step forward in time would enhance our military capability by having information before it happens. Intelligence Preparation of the Battlespace (IPB) has long been a major tenet of any military operation or campaign. This has been further refined to EIPB, or Environmental IPB. A submarine needs to know how sound will propagate in an ocean that may be cooler than normal or more saline. A cruiser or carrier radar must operate to its maximum range regardless of temperature or humidity. It is necessary for all warfare platforms and units to have knowledge of threat detection as well as their own detection. Sailors and officers can know this beforehand and during execution if they have reasonably accurate information on what the environment is and will be. The detail of that information is what may make the difference.

Concepts of Operations, with regard to systems that depend on radio frequency (radar and communications) and electro-optical (visible and infrared) propagation, often lead to increased importance for prediction of the small scale properties that affect systems' performance. This is the obvious case for planning but is also the case for execution phases since platforms or unit operations limit *in-situ* observations. Studies have already been conducted in several regions around the world, and under fleet exercise or field test scenarios, addressing environmental parameters that will impact propagation through the atmosphere. Frederickson et al. (2000) compared operationally realizable bulk estimations of the refractive index structure parameter with derived estimations from measured infrared (IR) scintillation over waters off San Diego. Hermann et al. (2002) looked at the changing horizontal structure of refractivity in Australia and its influence on propagation using numerical modeling. Willoughby et al. (2002) used radiosondes over numerous years in Nigeria to detect seasonal averages of refractivity gradients and K factors, while Atkinson et al. (2001) used different initialization schemes to find if a non-hydrostatic numerical model would accurately depict ducting situations over the Persian Gulf. And Tsuda et al. (2001) compared radiosonde soundings to a dual-system middle-

upper atmosphere radar and radio acoustic sounding system (RASS) to determine specific humidity profiles above 1.5 km in Japan. One common denominator among these studies, and all others, is resolution.

Higher resolution models, whether increased spatially or temporally, require evaluation before they are considered to be the answer for improving estimations of impacts on radar and optical propagation. For decades meteorologists and mathematicians have sought higher spatial resolution in numerical models. Pinpointing that one front to the kilometer or verifying the exact temperature inversion height down to the meter has, for some, been the final hurdle in forecasting. With modern advances in information technology and computing, it would seem we are not far from that goal. But even with these advances, will it make our forecasting better? Even if our forecasting does improve in the spatial scale, that may or may not necessarily increase our ability to predict detailed atmospheric impact on such things as optical scintillation and radar propagation. The latter, with regard to its sensitivity to changing horizontal resolution, will be the focus of this thesis.

B. BACKGROUND

A recent U.S. Navy fleet experiment off the southern California coast enabled evaluations of results from a high-resolution numerical model relative to representative *in-situ* meteorological measurements. The fleet exercise occurred in the vicinity of San Clemente Island, Ca. at the beginning of October 2004. Numerous rawinsondes were launched and continuous surface layer measurements were made from a small vessel, and atmospheric features and variations were compared with and matched against the U.S. Navy's Coupled Ocean/Atmosphere Mesoscale Prediction System (COAMPS®). As part of the Meteorology Department at the Naval Postgraduate School (NPS), the Boundary Layer Studies Group was interested in the propagation prediction possible with data from a higher-resolution (3-km) numerical model over typical, operational model resolutions of the day (9-km) and the impacts it may or may not have on estimating atmospheric effects in the Marine Boundary Layer (MBL). MBL properties obtained from a very complete collection effort will be used to evaluate the appropriateness of COAMPS® 3-km predictions for both planning and execution phases.

Figure 1 shows the data/model framework in which *in-situ* and predicted data sources can be applied to assessing the impact of the MBL on electromagnetic (EM) and electro-optical (EO) propagation. Turquoise highlighting shows what parts of the assessment process were used in this research with red lettering used to show the specific items utilized. The top row, Area I, shows the beginning of the integration process with different resources for predicted and measured information on the MBL. Area II represents the connection of data-gathering platforms with tactical operations centers ashore so as to build a Common Operating Picture (COP). Area III is the transforming of surface layer and upper air conditions into continuous or point environmental fields to feed into visualization schemes. Area IV shows the propagation modeling stage (e.g. APM, EOSTAR), while the last area lists the final integration of effects models (e.g. AREPS, *Builder*, and TAWS). The propagation models convert meteorological and radar parameters into ray tracing schemes and field strengths while the effects models quantify the impact on EM and EO propagation numerically and graphically.

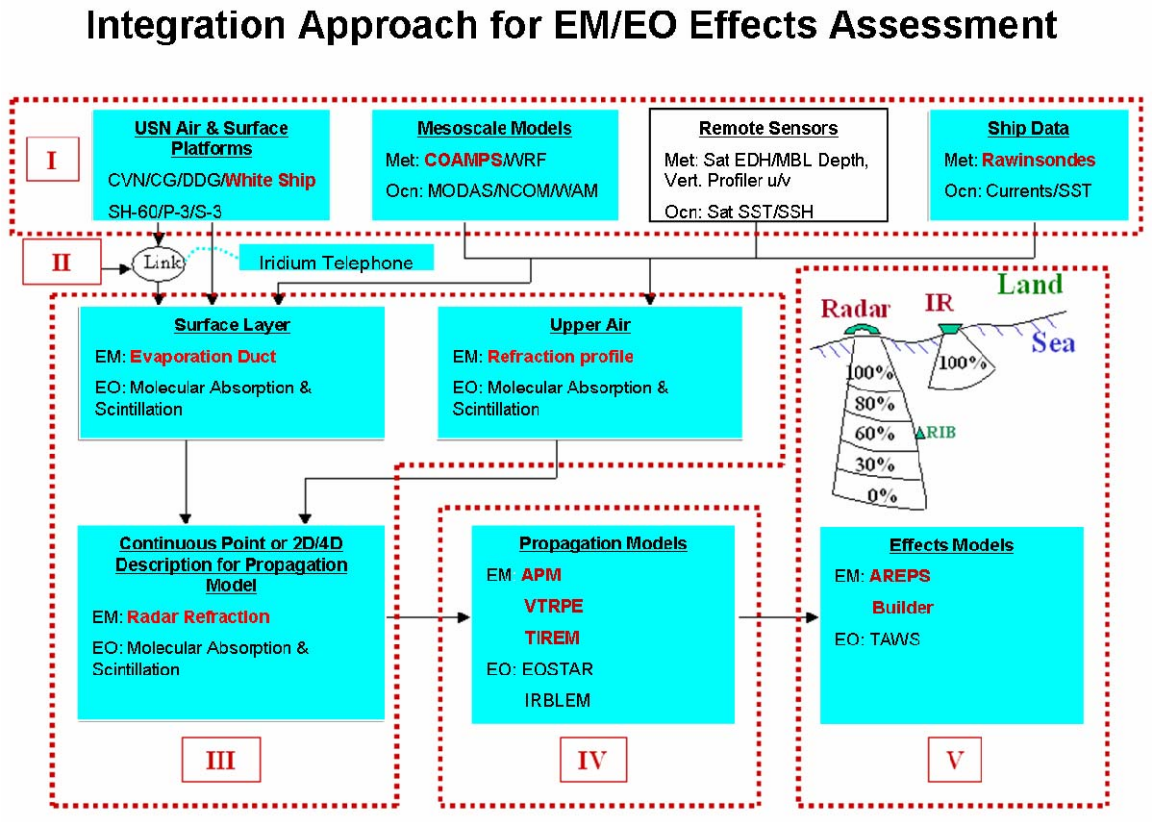

Fig. 1. EM/EO Effects Integration Flowchart

1. Atmospheric Effects on EM/EO Propagation

Atmospheric impacts on propagation can be caused by gaseous and particulate absorption of energy or by molecular refraction, altering the wave-front's orientation and causing distortion. Temperature and humidity change horizontally and vertically in the atmosphere. Vertical thermal and humidity gradients, together with buoyancy effects and wind mixing, can make these changes happen over shorter (longer) periods of time and smaller (larger) areas of space than usual. These changes will affect refraction and how waves propagate in the atmosphere through varying mean gradients, for radar and optical waves, and through turbulence-caused inhomogeneities, for optical waves.

a. Index of Refraction

Refraction is the bending or tilting of a sound or EM wave-front as it propagates through a medium with spatially varying characteristics. The index of refraction (n) is the ratio of speed of a wave in a vacuum (c) to the actual speed of a wave through a medium (v). These quantities are so close to each other in the lower atmosphere that they produce a value of n very close to one. Frederickson et al. (2000) used the following expression, dependant on wavelength and meteorological parameters, to describe visible and near-IR wavelengths:

$$n = 1 + 10^{-6}\{ m_1(\lambda)P/T + [m_2(\lambda) - m_1(\lambda)]\, qP/T\varepsilon\gamma \} \quad (1)$$

where T is temperature (in K), P is atmospheric pressure (in hPa), q is the specific humidity (in g g^{-1}), m_1 and m_2 are functions of the wavelength λ, ε is the ratio of ideal gas constants for dry air to water vapor (0.62197), and γ is a function of q. To analyze small differences from one, refractivity (N) is used. It is calculated by:

$$N = (n - 1) \times 10^6 = (c/v - 1) \times 10^6 \quad (2)$$

For radio waves, it is given by Bean and Dutton (1968) in terms of temperature (T), vapor pressure of moist air (e), and total atmospheric pressure (P):

$$N = 77.6\ P/T - 5.6\ e/T + 3.75 \times 10^5 (e/T^2) \quad (3)$$

The importance of humidity, as given by vapor pressure (e), for radio frequency propagation is apparent in the large coefficient ($3.75\ 10^5$) of the last term in Eqn (3). The significance of temperature in determining the refraction of optical waves and of

humidity in determining EM refraction is clearly evident in Figure 2. The two schematics on the left show the dependence of optical N on temperature and the two on the right show the dependence of radar N on e.

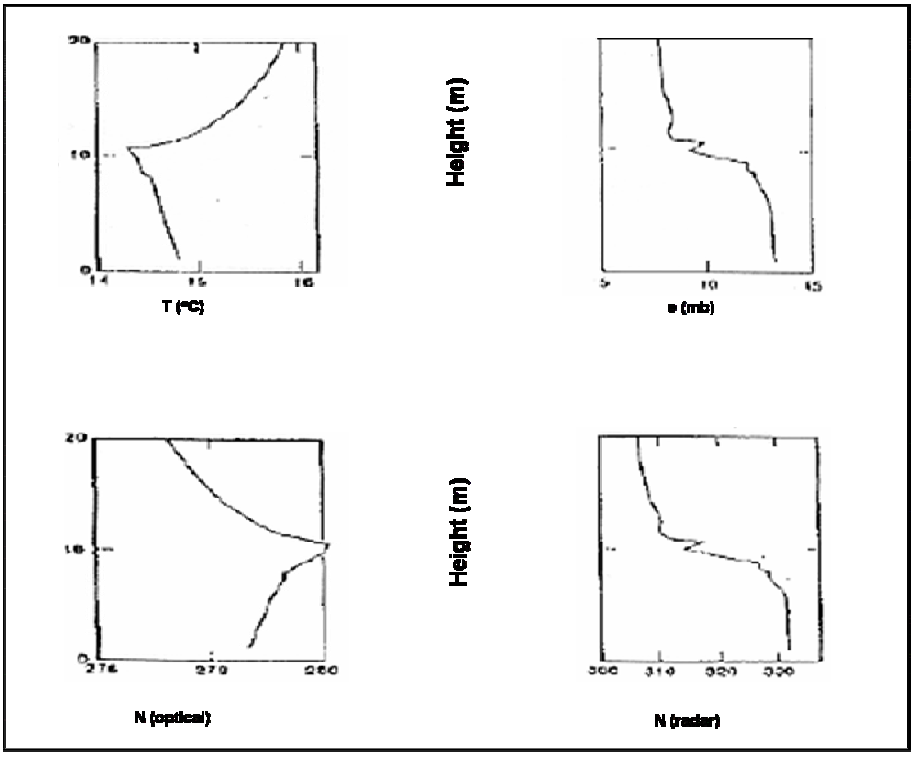

Fig. 2. Temperature and vapor pressure effects on N. Optical N dependence on T is shown on the left; radar N dependence on e is shown on the right.

b. Refraction and Radar Range/Loss

From Eqn (3), the gradient of N depends on the height (z) dependence of p, T and e. The vertical gradient of N describes EM wave ray geometry. For example, the distance to the horizon is given by:

$$d = \left[2 \times z / \left(r_e + \frac{dN}{dz} 10^{6)} \right) \right]^{1/2} \tag{4}$$

where d is horizon distance, z is height, and r_e is the earth's radius. This assumes, however, homogeneity in the horizontal with respect to the N gradient.

Wave fronts tilt in the atmosphere toward higher values of N. When dN/dz is positive (N increasing with height), the horizon distance is reduced since waves are

bent upward and away from the earth toward space. This is known as subrefraction. Causes for subrefraction would be onshore flow of marine air above a dry surface layer or the advection of saturated, warm air over cool waters. When dN/dz is less than zero (N decreasing with height), normal refraction occurs and waves are bent down toward the earth's surface. A phenomenon called trapping occurs when dN/dz is less than -0.157 m^{-1}. In this instance, refraction is so strong that EM waves are bent toward the earth with a radius of curvature less than the earth's radius. Under certain conditions, the waves are reflected off the earth back into the lower atmosphere, and then refracted down again to the surface where the process continues, forming a wave guide immediately above the surface. This can take place in the surface layer or in an elevated trapping layer above the surface. In transition zones of the atmosphere between different refracting layers, dN/dz can equal zero. In this case, the bending of the EM wave's path is equal to the earth's curvature and no refraction occurs relative to the surface. Figure 3 shows different refraction categories.

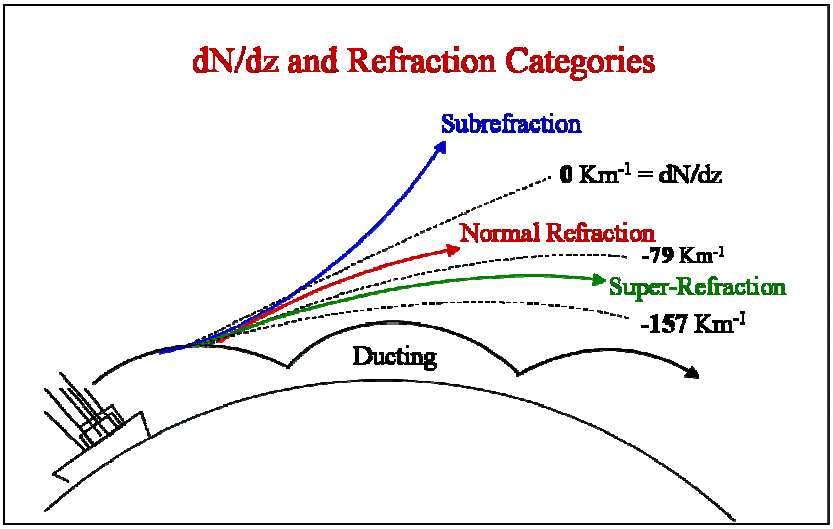

Fig. 3. Refraction Categories and dN/dz.

A modified refractive index (M) was created to show the refractive ray relative to the earth's surface. M is simply the refractive index (N) minus the dN/dz gradient for atmospheric trapping multiplied by the height in meters:

$$M = N + 0.157*z \quad (5)$$

Negative M gradients correspond to levels of trapping in the atmosphere. A positive gradient will show levels of EM waves escaping the atmosphere, and a zero M gradient will show levels of neither trapping nor escaping.

c. Ducting

A duct is the wave-guide associated with a trapping layer. The trapping layer constitutes the top of the duct, and the bottom of the duct is either the surface or the level at which an M value occurs equal to the trapping layer minimum. Ducts can occur at one level or multiple levels in the atmosphere. When a duct occurs immediately at the surface, it is usually due to evaporative effects and is called an evaporation duct. The evaporation duct height (EDH), indicating the duct's extent above the surface, is a parameter that will be analyzed later. Notice from Eqn. (3) that large increases in temperature or rapid decreases in water vapor pressure will produce the necessary drop in N to obtain negative gradients. Rapid decreases in water vapor are almost always the case over the ocean, particularly with high sea surface temperatures (SST). Figure 4 shows the evaporation duct at the bottom of both M profiles.

A surface-based duct occurs when a duct associated with a trapping layer extends to the surface. Excluding the evaporation duct, the main feature of the surface-based duct is that the minimum value for M aloft is less than the surface M value, as shown in Figure 4 as the red profile and upper portion of the blue profile. The values for M can either increase or decrease with height from the surface M value.

An elevated duct is one in which the ducting layer is not connected to the surface. In such a case, a local minimum value for M occurs above a local maximum. Below the local maximum, the values for M continue to decrease with decreasing height and fall below the local minimum value. Processes that can cause surface-based ducts are subsidence of dry air, increasing its temperature as it sinks, and offshore flow of dry air above a moist surface layer. Figure 4 shows the typical profile for an elevated duct in blue.

d. Propagation Loss

As the name implies, propagation loss is the amount of signal strength lost in an EM wave as it propagates away from its point of origin. It can be measured as the ratio of

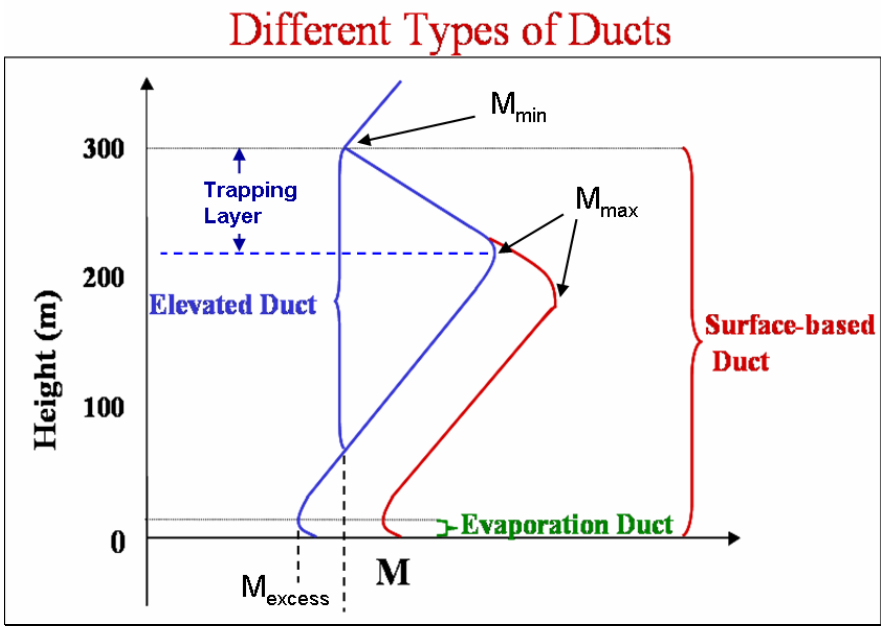

Fig 4. Examples of typical ducting profiles.

transmitted power to received power or as the difference between free space loss and propagation factor. Barrios (2003) used the latter description within the Advanced Propagation Model (APM), discussed in a later section, in the following equation:

$$L = 20 \log \{ 4\pi r / \lambda \} - 20 \log F \qquad (6)$$

where L is propagation loss, r is range from the transmitter, λ is the wavelength, and F is the propagation factor. The propagation factor is the ratio of actual field strength at a given point to free space field strength. It is evident from this equation that propagation loss increases with range and is inversely proportional to wavelength.

Propagation loss is instrumental in determining detection ranges of targets, whether "low-slow flyers", "high-fast flyers", or surface targets. Each type of target has its own corresponding radar cross section (RCS). RCS and measured or predicted prop loss can be used to calculate detection thresholds for targets. An advantage to using propagation loss and detection threshold is that they both are easily understood conceptually and visually. Figure 5 shows predicted prop losses for a transmitter at 20 feet above ground level (AGL) within a surface-based duct for four different transmission frequencies. If, for example, an aircraft were flying at the first height graduation of 100 feet and its RCS dictated 150 dB for detection (the orange color range), increasing

frequency on a radar transmitter from 1 GHz to 18 GHz would decrease the aircraft's detection range from roughly 19 NM to 14 NM. In the world of naval tactics, this change of five NM could be the difference in life or death.

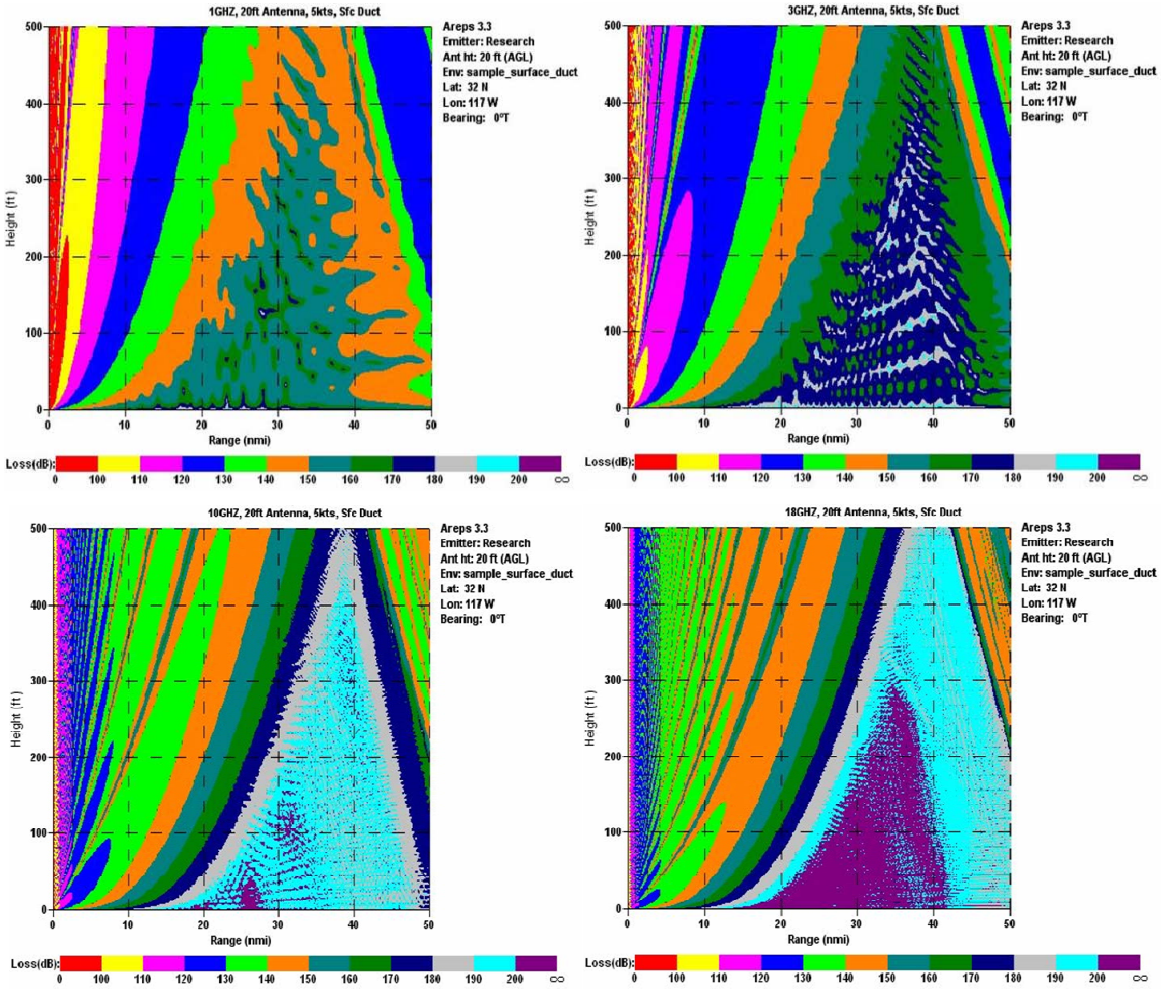

Fig. 5. Propagation loss (in dB) vs. height (in ft) and range (in NM) for 1 GHz (upper, left), 3 GHz (upper, right), 10 GHz (lower, left) and 18 GHz (lower, right) for 20-ft transmitter height within a surface-based duct.

e. Scintillation

Whereas the gradient of refraction and the resulting ray radius describe the overall impact of the atmosphere on radio waves, the refractive index structure parameter (C_n^2) quantifies the effect of small scale variations of index of refraction on an EM wave front along its path. It is simply a measure of the variability of n. These resulting micro-scale distortion effects on a wave front, as seen by twinkling lights at night or blurred objects viewed above a hot surface during the day, are illustrated in Figure 6. In an ideal

environment, wave fronts would propagate with no distortion. However, variations in pressure, temperature, or humidity will alter EM wave fronts and make them "wiggle" more. The impact of C_n^2, also called scintillation, on sensor performance includes image resolution for optical surveillance systems and beam spreading/wander for radar

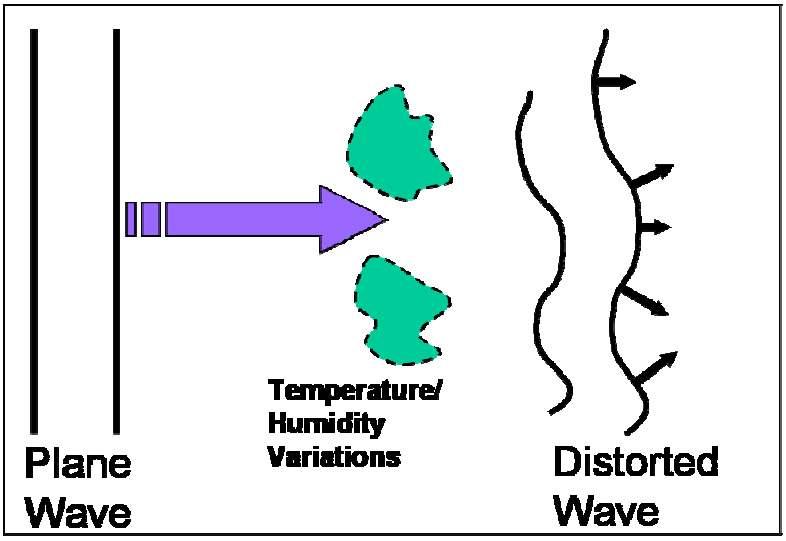

Fig. 6. Example of scintillation.

target designation systems. The general equation for C_n^2 is as follows (Andreas 1987):

$$C_n^2 = A^2 C_T^2 + A B C_{Tq} + B^2 C_q^2 \quad (7)$$

where A is defined as $\partial n/\partial T$, and B is defined as $\partial n/\partial q$. C_T^2 and C_q^2 are the temperature and humidity structure parameters, respectively. C_{Tq} is a cross-structure parameter of temperature and humidity. Each structure parameter can be defined for any variable x, in this case temperature and humidity, and is of the form:

$$C_x^2 = \langle x'(0) - x'(d) \rangle^2 / (d^{2/3}) \quad (8)$$

where d is a distance separating two fluctuation values. Each fluctuation value, annotated as x' at zero and x' at distance d, is a fluctuation from the ensemble time average. The angle brackets denote this time average within the MBL.

Turbulence in the MBL, which mixes and moves the aforementioned micro-scale variations, results in image blurring which has to be quantified to describe its

overall degrading effect on sensor performance (Driggers et al., 1999). The atmospheric Modulation Transfer Function (MTF) characterizes this degradation. The MTF is a reduction of contrast, i.e. white and black columns on a bar chart, as a function of spatial frequency. An expression for MTF, or image resolution, is:

$$MTF(\xi) = e\text{^}[-57.53\ \xi^{5/3}\ C_n^2\ \lambda^{-1/3}\ R] \tag{9}$$

where R is expressed as:

$$R = 0.2182*(\text{target size})^{5/8}\ \lambda^{1/8}\ (C_n^2)^{-3/8} \tag{10}$$

Here λ again is the wavelength but ξ is a function of range, R, and target size.

Monin-Obukhov Similarity (MOS) theory enables turbulent parameters in the surface layer of the MBL to be related to air-surface differences. A MOS-based bulk method uses single level airflow values for T, q, and u and a surface value for temperature, i.e. SST, assuming a surface relative humidity of 98%. Using the bulk method allows an estimation of C_n^2. See Frederickson et al. (2000) for further equations and analysis of their iteration scheme.

2. Trident Warrior/Silent Hammer

A field-based opportunity to evaluate COAMPS® predictions versus *in-situ* measurements of the meteorological variables mentioned above occurred in October of 2004. U.S. Naval forces at that time conducted a dual-purpose fleet exercise off the coast of southern California. TRIDENT WARRIOR is an annual ForceNet sea trial experiment sponsored by NETWARCOM. Its mission was to provide a rapid fielding of technology and tactics to the fleet. Concurrent with TRIDENT WARRIOR was SILENT HAMMER. Its mission was to demonstrate the ability of a submarine to act as a Joint Operations platform for intelligence collection and time-sensitive strikes (http://www.afcea-sd.org/briefs/june15_2004.ppt#2).

Within this exercise framework, personnel from the Fleet Numerical Meteorology and Oceanography Center (FNMOC) and NPS combined their data collection and analysis with that of personnel from the Naval Research Labs (NRL). A small boat, the Research Ship (R/S) Acoustic Explorer, remained in the vicinity of San Clemente Island and gathered meteorological data utilizing rawinsondes and the ship's own data

collection system. This data was sent via iridium telephone link to NPS. It was used in boundary layer bulk model calculations initially and also plotted for ease of use. From there it was relayed to FNMOC, pushed to the Classified level, and posted to the SIPRNet. NRL personnel, located on the USS Tarawa and USS Georgia, were then able to gather the necessary meteorological data points for infusion into the *Builder*™ software (D. Keeter 2005, personal communication).

3. Meteorological and Propagation Models

Different modeling programs were used in the course of this thesis with different outputs in mind. The main purpose has been an analysis of the high-resolution mesoscale model. EM propagation models were also used to show the sensitivity of atmospheric propagation to meteorological parameters.

a. High-Resolution COAMPS®

The Coupled Ocean/Atmosphere Mesoscale Prediction System (COAMPS®) is a mesoscale model developed by the Marine Meteorology Division of NRL (Hodur, 1997). The atmospheric portion of the model uses the non-hydrostatic, fully compressible equations of motion. There are prognostic equations for momentum, non-dimensional pressure perturbation, potential temperature, turbulent kinetic energy, and mixing ratios of water vapor, rain, snow, clouds, ice, and grauple. COAMPS® also contains advanced parameterizations for surface and boundary layer processes, radiation, moist physics and convection. It has two main components – analysis and forecast.

An analysis field is generated first from multiple data sources. COAMPS® uses global forecasts from the Navy Operational Global Atmospheric Prediction System (NOGAPS) for boundary conditions. Observations from satellites, aircraft, surface and upper-air stations, buoys and/or ships are input along with previous COAMPS® 12-hr forecasts, if available. It calculates a "first-guess" field from these data sources using a multi-variate optimal interpolation (MVOI) scheme. From here COAMPS® performs a time-integration using its programmed equations and 3-D model physics to produce hourly forecast fields. In this set of data, hourly fields are output from four consecutive 12-hr forecasts initiated at 0000 UTC on October 5th of 2004. Two runs are performed at 0000Z and 1200Z for each day of interest. The sea surface temperature (SST) field, although a boundary condition, is held constant for each 12-hr forecast.

COAMPS® uses horizontally programmable, nested grids. In our data collection, there are three grid resolutions (27-, 9- and 3-km) that center around the Southern California (SoCal) region. See Figure 7. The 3-km and 9-km grids will be used for our

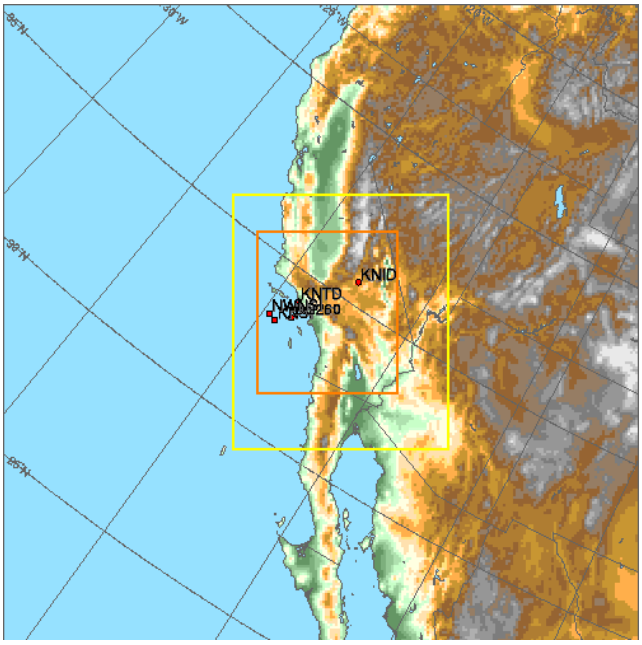

Fig. 7. COAMPS® grids for Southern California. Orange box is 3-km resolution, yellow box is 9-km resolution, and the entire figure is 27-km resolution.

data analysis. Horizontal resolution can be as high as only a few hundred meters, but consideration must be given to computer time as well as operational efficiency. The analysis is performed on the Arakawa-Lamb scheme A grid, which means no staggering of values. The forecast model grids are staggered both in the horizontal and vertical. For the horizontal forecast grids, the Arakawa-Lamb scheme C grid is used (Long, 2003). Vertically, COAMPS® calculates analysis and forecast variables on terrain-following sigma levels. This is helpful for measurements that must remain at a certain height above the surface. Since we were interested in comparing bulk evaporation duct model calculations over the ocean with different data sources, the first sigma level of 10 m will be used for air values. COAMPS® can have up to 300 sigma levels but only 30 are used here.

b. NPS Bulk Model

The NPS bulk evaporation duct model computes vertical profiles of air temperature and humidity from single input values of wind speed, air and sea temperature, relative humidity and pressure from which modified refractivity profiles and the evaporation duct height are calculated. Frederickson and Davidson (2005, manuscript submitted to *J. Appl. Meteor.*) explain the basics of MOS theory, upon which the NPS bulk model is based, and present the model's fundamental equations. Only a short synopsis of the model is given here.

Within the surface layer, which generally extends upward between 10 and 100 m above the surface depending on conditions, turbulent fluxes of momentum, sensible heat, and latent heat are assumed constant with height. In addition, horizontal homogeneity is also assumed. The NPS evaporation duct model uses the TOGA COARE model version 2.6 (Fairall et al., 1996) to calculate scaling parameters for wind speed, potential temperature, and specific humidity. They are defined according to the assumed-constant, near-surface fluxes as follows:

$$u_* = - \langle w'u' \rangle^{1/2} \tag{11}$$

$$\theta_* = - \langle w'\theta' \rangle / u_* \tag{12}$$

$$q_* = - \langle w'q' \rangle / u_* \tag{13}$$

where, as before, the brackets denote an ensemble time average and primed quantities are fluctuations from that average. It is here that the use of the TOGA COARE model ceases. The scaling parameters, along with height z and the buoyancy parameter g/θ_v, are then combined into a 'stability' ratio, ξ:

$$\xi = z/L = (zkg\,[\theta_* + 0.6078\theta_* q + 0.6078 T q_*]) / \theta_v u_*^2 \tag{14}$$

Here L is not prop loss but the Obukhov length scale and k is the von Karman constant (0.4). The stability ratio, not to be confused with ξ in section 1.e on scintillation, is input to stability-dependent profile functions (ψ_U, ψ_θ, ψ_q) for computing vertical profiles of wind speed, potential temperature and specific humidity from the following equations:

$$U(z) = U_o + u_*/k\,[\ln (z/z_{oU}) - \psi_U(\xi)] \tag{15}$$

$$\theta(z) = \theta_o + \theta_*/k \, [\ln (z/z_{o\theta}) - \psi_\theta(\xi)] \quad (16)$$

$$q(z) = q_o + q_*/k \, [\ln (z/z_{oq}) - \psi_q(\xi)] \quad (17)$$

where z_{oU}, $z_{o\theta}$, and z_{oq} are momentum and scalar roughness lengths. Frederickson and Davidson (2005) cite Smith (1988) for the z_{oU} equation. This equation is a function of u_*, the Charnock constant, and the kinematic viscosity of air. In accordance with Smith (1988) and Fairall (1996), the NPS model uses a value of 0.011 for the Charnock constant, representing deep water and open ocean conditions with wind and surface wave fields in coordinated equilibrium. Bradley et al. (2000) provide a function for $z_{o\theta}$ and z_{oq} based on u_* and z_{oU}.

Eqs. (11) to (17), in addition to the stability function equations not shown here, form a closed system. An iterative process, beginning with mean values for u, T_{air}, SST, and q, is used to obtain the scaling parameters θ_* and q_*. These scaling parameters help to calculate profiles for T and q, which in turn are used to calculate the profile of the partial pressure of water vapor, e. The vertical profile of pressure is estimated by integrating the combined hydrostatic equation and the ideal gas law. Now that profiles exist for P, T, and e, modified refractivity (M) can be calculated from Eqs. (5) and (3) and an evaporation duct height determined by finding the height of the local minima in M nearest the surface. Frederickson and Davidson (2005) limit their profile calculations to the first 50 m of the atmosphere, which is assumed to be encompassed within the surface layer for all stabilities. The NPS bulk model is very sensitive to the atmospheric stability, as seen in Figure 8.

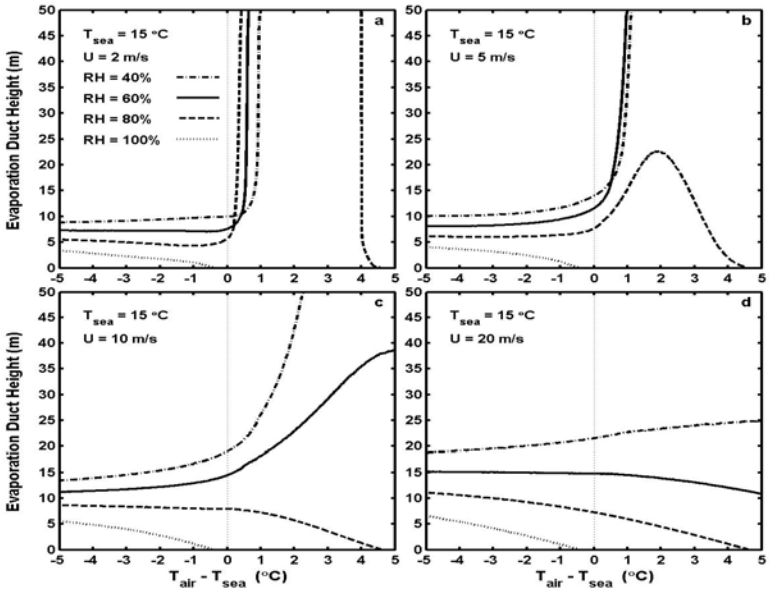

Fig. 8. NPS bulk model dependency on Air-Sea Temperature Difference (ASTD) in calculating evaporation duct height (EDH) for changing wind speed and relative humidity conditions.

c. AREPS (APM)

The Advanced Refractive Effects Prediction System (AREPS) is a follow on EM propagation prediction software package to the Integrated Refractive Effects Prediction System (IREPS). Both were developed by the Space and Naval Warfare Systems Center, San Diego (SPAWAR). AREPS is a Graphics User Interface (GUI) in which a user can input environmental and radar system information to the Advanced Propagation Model (APM) for generating two-dimensional views of propagation loss, vertical M-profiles, and propagation condition summaries from model calculations. It can model the propagation impacts of pre-loaded 2-D and 3-D radars and use preloaded environments, such as a standard atmosphere or elevated duct, and also import specific environments from rawinsonde data or models, such as COAMPS®. AREPS also has incorporated the NPS evaporation duct model for computing near-surface M profiles from specified input parameters.

APM is valid for the 100 MHz to 20 GHz frequency range. It is a combination of the Radio Physical Optics (RPO) model, discussed in a later section, and the Terrain Parabolic Equation Model (TPEM). It was designed out of the necessity to

incorporate a better terrain-influenced EM model since FFACTOR, the model used in IREPS, was for over-ocean areas only and did not take into account terrain effects (Barrios 2003).

APM begins by running the Parabolic Equation (PE) algorithm for propagation loss under a maximum propagation angle, which in turn dictates maximum ranges and heights. It then calculates propagation loss for other predetermined zones using three other algorithms. They are the flat earth (FE), the ray optics (RO), and the extended optics (XO) algorithms. The RO model is used for angles above the maximum PE propagation angle but less than 5^o elevation. The FE algorithm is applied for all heights and ranges out to 2.5 km from a source and elevation angles greater than 5^o. The XO model is then applied to areas above the PE region and outside the RO region. Figure 9 shows the different regions in the APM.

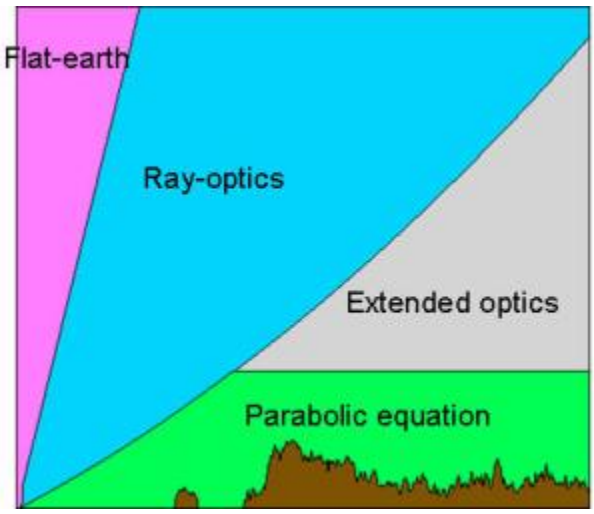

Fig. 9. Propagation regions in the Advanced Propagation Model (from Barrios, 2003).

The AREPS software then plots the propagation loss values in color-coded graphs for visual interpretation by the user. Figure 5 contains propagation loss diagrams generated by AREPS. A handy tool in the AREPS software is its ability to model different radar types and frequencies. Given its ability to also incorporate alternative meteorological environments, there are literally thousands of scenarios that can be modeled.

d. Builder™

The *Interactive Scenario Builder 3* (*Builder*) is an interactive, 3-D tactical decision aid (TDA) for RF propagation. It is a joint venture between Remcom, Inc. and NRL. *Builder* operates in the EM Propagation Integrated Resource Environment (EMPIRE) to utilize different EM propagation models which may or may not be written in different computer code. It uses Digital Terrain Elevation Data (DTED), U.S. Air Force and Navy weather data, NGA map products for visualization, complex antenna pattern information, multiple radar cross sections, and other data sources (Remcom, Inc., 2003). *Builder* can generate horizontal or vertical depictions of signal to noise ratio (SNR), signal strength, EM jamming effects, and target tracking. It also allows the system user to input new aircraft or ship platforms, different transmitter parameters, changing platform positions, and altering ducting environments. *Builder* can even generate moving depictions in time and space of changing variables for complex and multiplatform operations to help commanders and team leaders better visualize EM system performance and degradation. Figure 10 shows *Builder* horizontal output screens for changes in the ducting environment, while Figure 11 shows a vertical cross-section difference between a no-ducting and ducting situation.

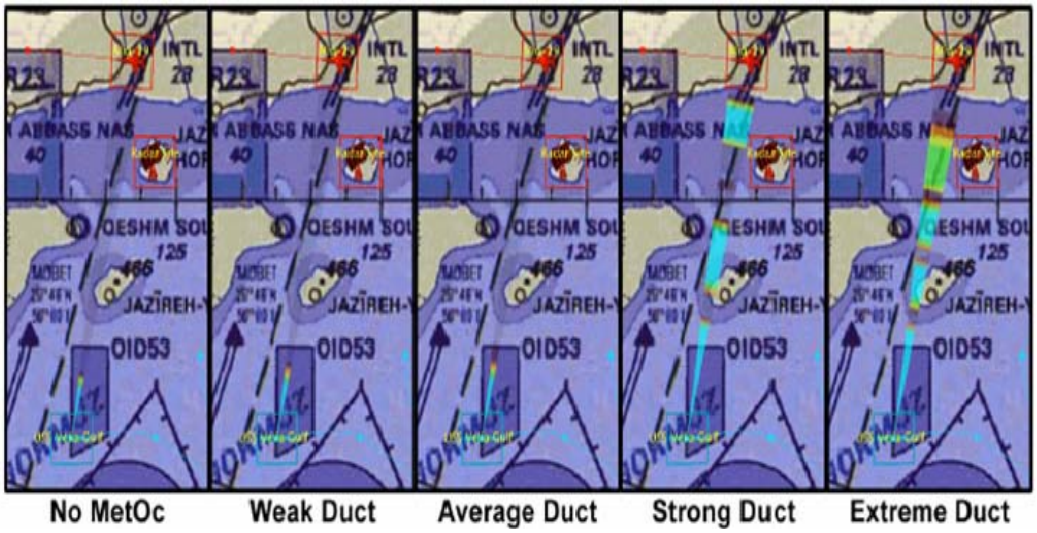

Fig. 10. *Builder* METOC effects on radar (from NRL, 2003).

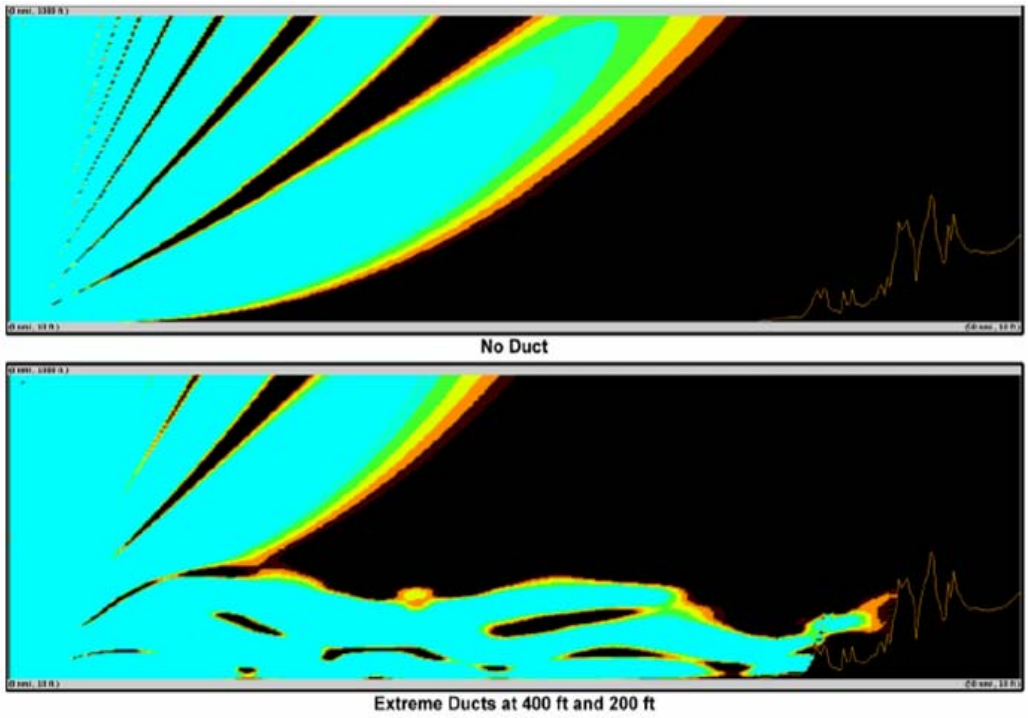

Fig. 11. *Builder* vertical cross-section of SNR without and with ducting environments (from NRL, 2003).

Operating in the EMPIRE allows *Builder* to reach into EM models such as RPO, Variable Terrain Radio PE (VTRPE), Terrain Integrated Rough Earth Model (TIREM), Freespace, and the millimeter wave (MMWave) model. RPO, VTRPE, and TIREM are quickly summarized below.

(1) RPO. The RPO model, used for the RF range from 100 MHz to 20 GHz, was created to speed up calculation times from those obtained using split-step PE methods. It separates an area into four regions, just like the APM. It also uses the same algorithms as APM. Since RPO was created first, it does not take into account environmental effects. Rather, it uses a vertical M profile located at the transmitter (Hitney, 2003). This is an obvious source for potential error in non-homogeneous environments.

(2) VTRPE. The VTRPE model is said to be "the most versatile and precise model found in EMPIRE" (Remcom, Inc., 2003). It can model the ionospheric sky wave, terrain reflection and diffraction, ducting, and the ground wave. It is a full PE with no approximations nor hybrid methods used. This bears proof in the

longer run times obtained from *Builder* when using this method. The EMPIRE computes the atmospheric refractive index profiles for VTRPE which then uses those profiles and calculates ionospheric profiles if needed. Its Rf range is from 100 kHz to 100 GHz.

(3) TIREM. TIREM, operating from 2 MHz to 20 GHz, is a general purpose point-to-point model developed by the Joint Spectrum Center (JSC). Unlike some other models that assume the effective earth's radius (generally 4/3), TIREM uses the surface refractivity to calculate it. It can compute rain and foliage attenuation as well as model the ground wave, terrain reflection and diffraction, and troposcatter. Remcom, Inc. boasts that the JSC validation report has over 10,000 real-world measurements with a mean error less than 1 dB (Remcom, Inc., 2003).

(4) FFACTR. Formerly known as the Navy Standard Model, FFACTR was developed by SPAWAR prior to RPO. It was also used in IREPS, which was the predecessor to AREPS. It is valid from 100 MHz to 20 GHz and designed for over-water paths. It models ducting effects, reflection, diffraction, troposcatter and accounts for forward-reflected energy from surface roughness based on wind speed.

(5) MMWave. The millimeter wave propagation model is another model developed by the Joint Spectrum Center. MMWave applies terrain masking in its calculations and also takes into account atmospheric absorption. Its Rf range is 1 to 300 GHz and often used in satellite to ground path modeling.

(6) Freespace. Although there are technically two versions of the Freespace model used in *Builder*, we will use the one simply named Freespace which assumes a spherical earth.

II. DATA COLLECTION AND PROCESSING

A. HIGH-RESOLUTION COAMPS®

COAMPS® 3-km data was obtained from runs with a model used for development studies by the Geophysics Division of the Naval Air Warfare Center (NAWC) at Point Mugu Naval Station in San Diego. The high-resolution model data is not operational but comparisons have occurred between 3-km predictions by the NRL Meteorology Division (Monterey, CA) with *in-situ* evaporation duct descriptions by NPS. For this study, the NAWC-provided data was processed to obtain vertical soundings for parameters such as air temperature, pressure, water vapor mixing ratio, and modified refractivity. Each vertical sounding was co-located on the earth to the latitude and longitude of the launch point for each rawinsonde. It was also matched to the launch time of the weather balloons.

A UNIX script file temporally interpolated between appropriate forecasts and then spatially interpolated between grid points horizontally in the x- and y-directions for each sigma level. Two separate script files were written by Robert Creasey of the NPS Meteorology Department. One was used to read a modified time-series at the 10-m sigma level in COAMPS® from each of the 48 hourly forecasts. The other read MCSST values corresponding to the days and location of the exercise in October of 2004. MATLAB 7.0.4 code calculated different variables and generated plots for visual analysis. Professor Wendell Nuss, also of the NPS Meteorology Department, provided support with COAMPS® analysis through his VISUAL program. The analysis is shown in section III A.

B. RAWINSONDES

Balloon-borne radiosondes were used to obtain profiles of atmospheric variables through the MABL. The balloon-borne rawinsondes, Vaisala RS80-15L's, were launched from the R/S Acoustic Explorer and provided, according to time from launch in minutes and seconds, the measured wind speed and direction, temperature, dew point, relative humidity and pressure, and calculated height, ascent rate, refractive index, and modified refractive index. Figure 12 shows the launch locations in relation to San Clemente Island.

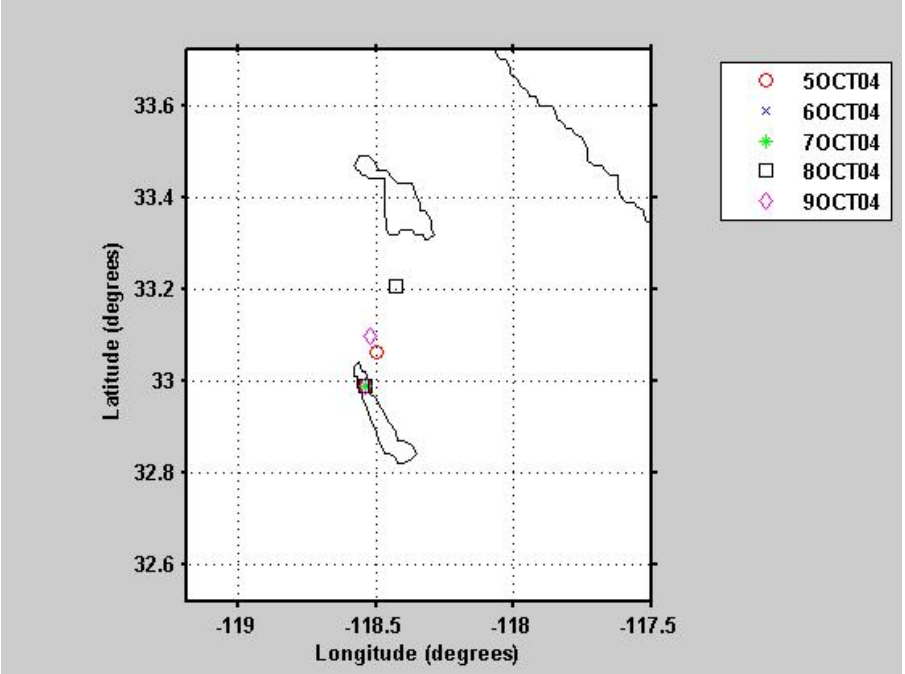

Fig. 12. Rawinsonde launch points in relation to San Clemente Island.

The rawinsondes, launched by METOC and Naval Special Warfare personnel, were calibrated to record the first data level at three meters in height. This introduces some error to the problem since some launches were more horizontal upon release, and thus closer to three meters, and some were more vertical upon release, and thus further away from three meters. Due to this uncertainty of the first level, the second data level from the rawinsondes will be used. The second data level ranged between three and nine meters. Following from the MOS theory and NPS bulk model discussed above, these values are most likely to be in the surface layer for each day. The vertical rawinsonde soundings are analyzed in section III A, part 2.

C. SHIP'S SURFACE LAYER AND SURFACE DATA COLLECTION SYSTEM

The vessel's data collection system provided date, GMT, latitude, longitude, true wind speed and direction, air temperature, barometric pressure, relative humidity, and

SST via an infrared (IR) probe. Two instrument packages, consisting of the same pieces of equipment, were placed on both the port and starboard side of the R/S Acoustic Explorer. Both systems provided simple ASCII text files, averaged every five minutes, which were used to calculate boundary layer variables. Figure 13 shows the R/S Acoustic Explorer and the location of the two sensor packages. Table 1 summarizes the equipment information.

Table 1. Summary of R/S Acoustic Explorer data collection equipment.

Acoustic Explorer MET-Station			
Parameter	**Accuracy**	**Instrument**	**Range**
NPS MET MAST Sensing System			
Wind Speed	± 0.5 m s^{-1}	Climotronics Sonic Anemometer	0 to 50 m s^{-1} ± 20° pitch or roll
Wind Direction	± 5°		
Air Temperature	± 0.2°	Rotronic MP 100H/400H Temperature/ Humidity Probe	-40 to 60°C
RH	± 1.5%		
Barometric Pressure	± 0.5 mb	AIR-DB-2A Barometer	-25 to 50°C 800 to 1060 mb
Boat Speed/ Position	± 0.1 kts ± 3 m	Garmin GPS 16/17	
NPS Sea Surface Temperature Sampling Systems			
SST	± 0.3° ± 0.2°	Campbell Scientific IRTS-P	5 to 45°C 15 to 35°C
NPS Sea Logging/Transmission System			
Data Logger		Campbell Scientific CR10X	

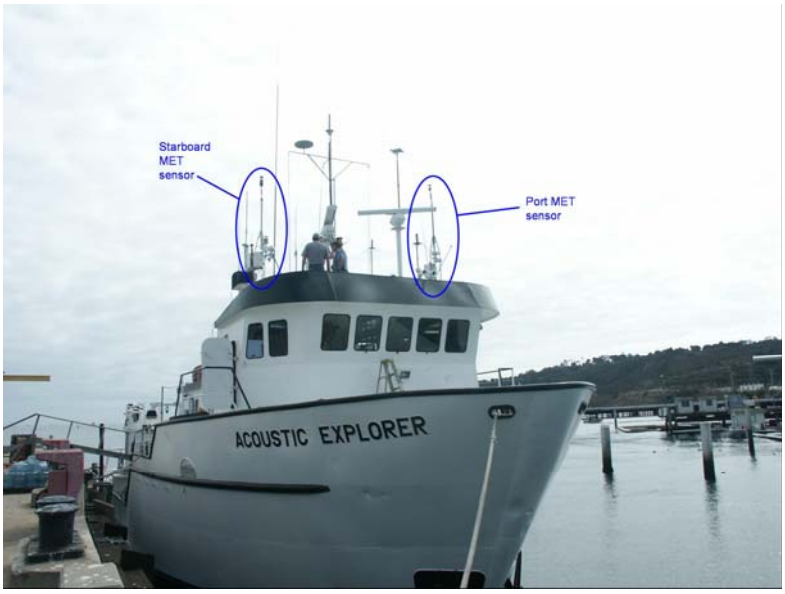

Fig. 13. R/S Acoustic Explorer with port and starboard sensor packages.

D. APPLICATION OF THE NPS BULK MODEL

After collecting data from the rawinsondes, each COAMPS® run, and the ship's data system, Paul Frederickson entered values via FORTRAN code into the NPS bulk model. The outputs are a sextuplet plot of wind speed, air and sea temperature, relative humidity, log C_n^2, EDH, and estimated detection range. The estimated detection ranges, calculated from the APM but not within AREPS, use the same inputs of 140-dB detection threshold and target size of two meters. Analysis is given in section III D.

E. EM MODEL PROCESSING AND OUTPUTS

1. AREPS (APM)

All 21 rawinsondes and corresponding 9-km and 3-km COAMPS® vertical soundings were input to AREPS as simple text files in column format. After calculating a propagation condition summary, as seen in an example in Figure 14, they were saved as individual environment files for later use. These environment files could then be used to

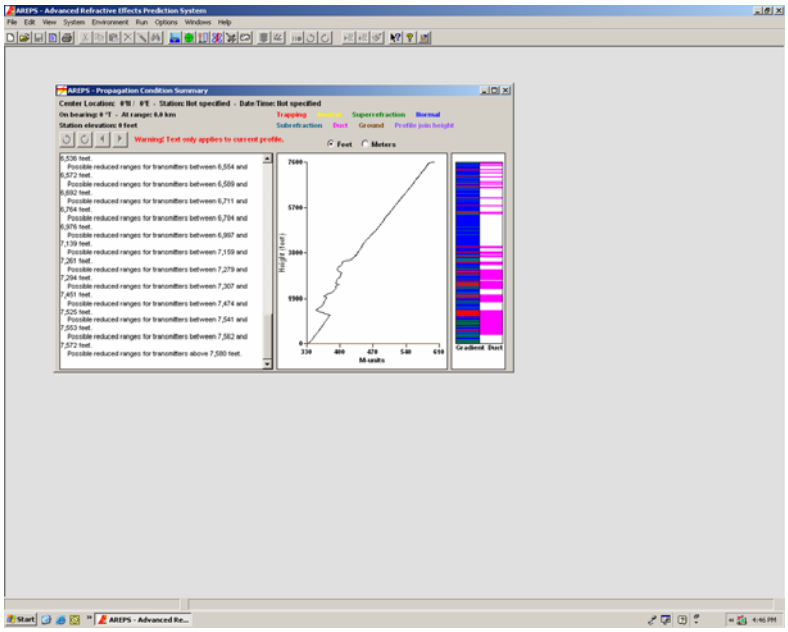

Fig. 14. Typical AREPS Propagation Condition Summary.

process different radar frequencies, evaporation ducts heights, elevated duct heights, transmitter polarizations, surface wind conditions, and the like. Each COAMPS® and rawinsonde vertical sounding was processed for four frequencies – 1, 3, 10, and 18 GHz. Analyses are given in section III B.

2. *Builder*™

NRL Monterey has a current version of the *Builder* software. The same COAMPS® and rawinsonde soundings were manipulated in the EM propagation models explained earlier within *Builder*. A separate scenario was constructed for all soundings for the four frequencies mentioned above. Analyses are given in section III C.

THIS PAGE INTENTIONALLY LEFT BLANK

III. RESULTS

A. METEOROLOGICAL COMPARISONS

1. Silent Hammer Synoptic Situation

A typical summertime, synoptic situation occurred during Silent Hammer. The Southern California offshore region was under the influence of the Easter Pacific High and an inland thermal low. Beginning on October 5th of 2004, the general atmospheric situation had a low pressure area that remained inland over southern California and western Arizona. See Figure 15. This inverse trough did not appear to deepen

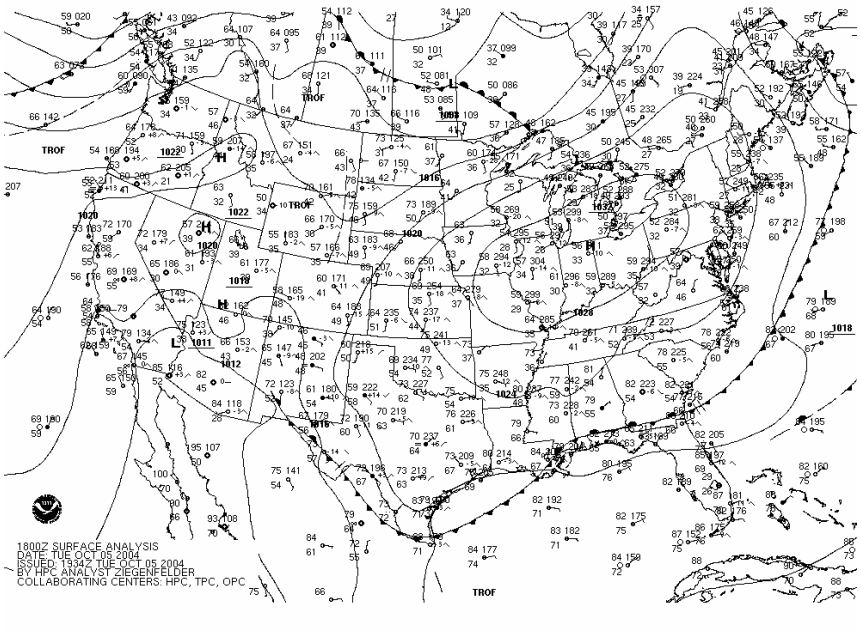

Fig. 15. NOAA surface analysis for October 5th, 2004 at 1800 UTC (high pressure area west of Southern California not shown).

significantly over the five day period, staying around 1010 to 1012 mb, and brought northerly to northwesterly flow around San Clemente Island. Based on an analysis of synoptic charts obtained from the National Oceanographic and Atmospheric Agency (NOAA) website, the most significant change in weather came on the 9th of October at 1800 UTC (Fig. 16). A cold front moved through the area which had been spawned off a low pressure system located northwest of Washington.

The northerly or northwesterly flow regime over San Clemente Island should bring drier air from over the Los Angeles and Vandenburg Air Force Base areas since it

will not have had enough time to become moist, over-ocean air. This dryness would cause or maintain an elevated ducting situation due to the lowering of the vapor pressure of moist air which in turn lowers N, as seen in Eqn. (2), near the surface. Lowering N near the surface would leave higher N values above and cause an elevated duct situation.

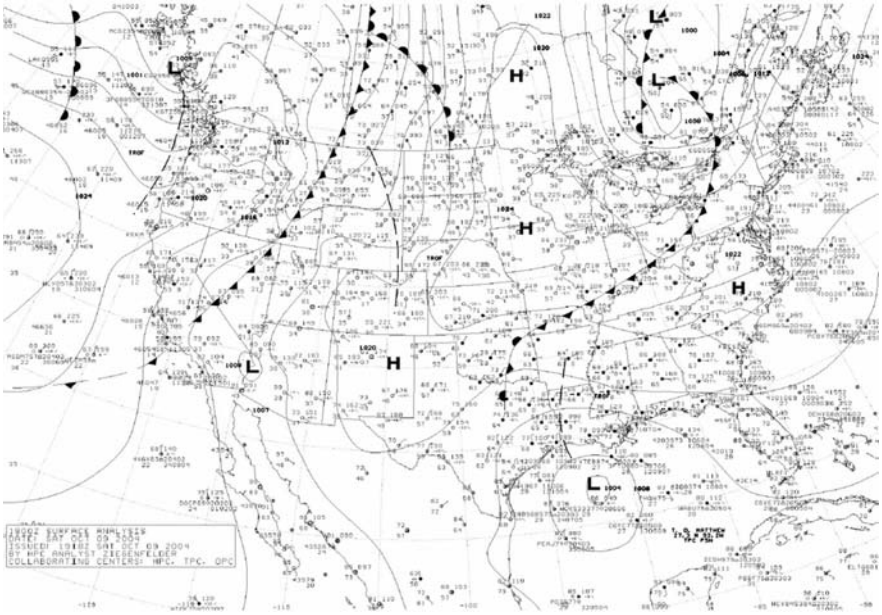

Fig. 16. NOAA surface analysis for October 9th, 2004 at 1800 UTC.

2. Rawinsondes and COAMPS® Obtained Soundings

Since we are mainly interested in the meteorological factors affecting EM propagation, we will focus on the temperature, relative humidity (or water vapor pressure), total atmospheric pressure, and M profiles obtained from radiosonde launches and predicted by COAMPS®. This excludes the vector wind and cloud conditions.

a. Pressure

As expected, COAMPS® did exceptionally well with pressure prediction. Because the hydrostatic assumption was the basis for assigning pressure heights in the radiosonde profiles, gradients of pressure change were highly accurate with no discernible differences. The root mean square (RMS) difference between 9-km COAMPS® and rawinsonde pressure values was between 1.31 and 1.96 mb for the 10-m sigma level through the 1600-m sigma level. The disparities for the 3-km COAMPS®

were larger at an RMS range of 6.38 to 8.44 mb. Both sets of RMS differences decreased with increasing height. Pressure gradient differences would have little impact on propagation prediction.

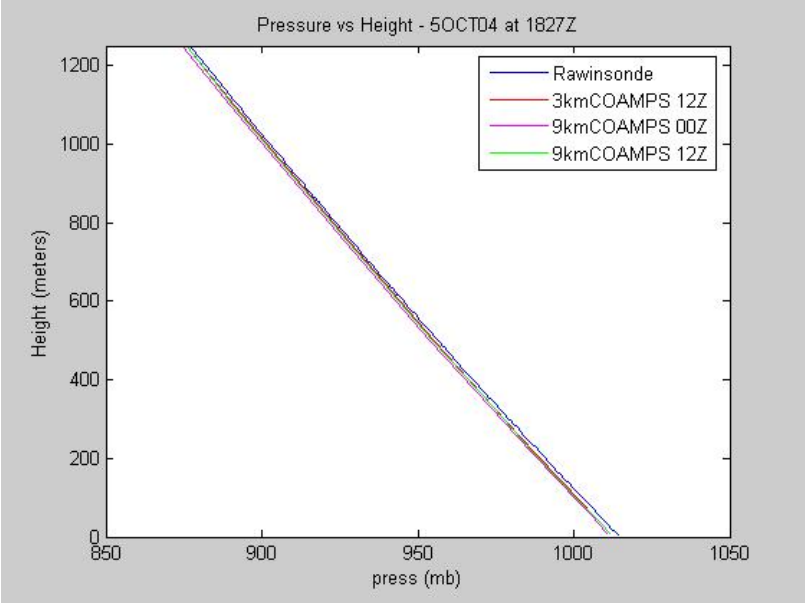

Fig. 17. Pressure (in mb) vs. height (in meters) for COAMPS® 9-km and 3-km interpolations and October 5th 1827 UTC rawinsonde.

b. Temperature

The COAMPS® temperature and relative humidity profile comparisons, however, showed differences that could affect EM propagation prediction. Overall, the 3-km and 9-km COAMPS® temperature gradients were in very good agreement with the rawinsonde temperature gradients. The temperatures from which the COAMPS® gradients started, however, were off by one to two degrees Celsius or displaced vertically by as much as 500 m. Figure 18 shows the temperature-height sounding comparisons for the same date and time as Figure 17. Notice how well the gradient for the rawinsonde (in blue) matches the COAMPS® gradients (in red, magenta and green) up to approximately 180 m in height. Although the profiles differ above the inversion, the gradients within the temperature inversion are in good agreement. The gradient for the rawinsonde (blue) between approximately 380 and 500 m appears parallel to the 9-km COAMPS® gradients (purple and green) between 330 and 500 m. The same can almost be said for the 3-km

COAMPS® gradient between 215 and 330 m within the temperature inversion, but the obvious height disparity is a concern. Other dates and times in which general shapes and gradients match are all profiles for October 6th, soundings on October 7th at 0221 and 0717 and 1901 UTC, all profiles for October 8th but the 1058 and 1510 UTC profiles, and the 1850 UTC sounding for October 9th. Profiles not included in this list were excluded due to the fact that only a portion of the profile's gradient did not correspond to the rawinsonde.

RMS temperature differences between the rawinsonde and each COAMPS® run were similar. These RMS errors are calculated from the spatially interpolated soundings extracted from the COAMPS® forecast fields. This means they can be calculated using anywhere from 6- to 19-hour forecasts. RMS errors between rawinsonde air values and COAMPS® forecast values for the corresponding times will be shown in a later section.

The RMS temperature differences between the rawinsonde soundings and 9-km COAMPS® were between 1.30 and 6.72°C. Interestingly, these RMS errors decreased with increasing height up to the 90-m sigma level. They then increased with increasing height up to the 330-m sigma level (a total of only three sigma levels) where they decreased again. The RMS differences between the rawinsonde and the 3-km COAMPS® were between 1.4 and 6.47°C. These increased with increasing height up to the 330-m level, decreased rapidly at the 500-m sigma level, increased at the 700-m level slightly, and then decreased with increasing height. Only three out of 11 sigma levels for the 3-km COAMPS® run had smaller RMS differences in temperature than the 9-km COAMPS® forecasts. The largest temperature RMS differences occurred for both the 9-km and 3-km resolution runs at the 330-m sigma level. These findings contrast the results of Wetzel et al. (2004) who found that increasing horizontal resolution from 3-km to 1-km improved two mesoscale models' ability to depict the inversion base height and cloud top height.

As for temperature accuracy in the vertical, there were three instances when COAMPS® missed the height of a temperature minimum or maximum point by 400 to 500 m. These occurred on October 5th at 1827 UTC, October 6th at 1831 UTC and

October 7th at 0717 UTC. The corresponding rawinsonde soundings showed elevated ducts for these days. There were four occurrences when height was off by 300 to 400 m, five occurrences for height differences of 200 to 300 m, eleven instances when off by 100 to 200 m, and twelve times when COAMPS® was inaccurate by less than 100 m.

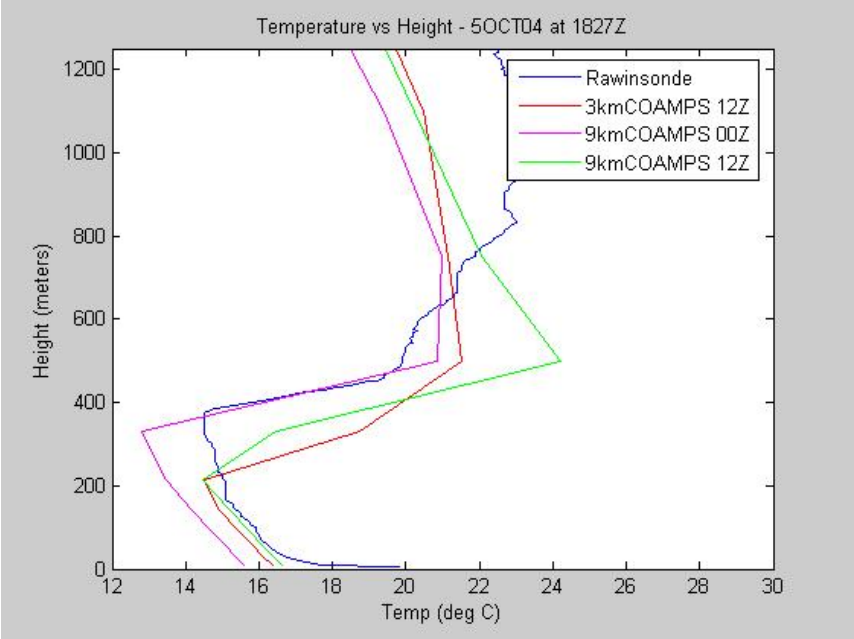

Fig. 18. Temperature (in degrees C) vs. height (in meters) for COAMPS® 9-km and 3-km interpolations and October 5th 1827 UTC rawinsonde.

c. Relative Humidity

Relative humidity profile comparison results are more difficult to describe and generalize. Upon initial inspection of the vertical soundings, RH readings appear to have more variability than the temperature readings at the same levels. Variations are noticeable in the temperature values but at much smaller vertical scales. This may be in part due to irregularities in the humidity sensor of the Vaisala rawinsonde or that the micro-scale humidity fluxes are more variable than the temperature fluxes.

The most notable soundings with regard to overall accuracy are from October 5th at 2250 UTC and October 9th at 2335 UTC, and are shown in Figs. 19 and 20 respectively. The 3-km COAMPS® profile at 2250Z on the 5th is extremely accurate up to approximately 215 m. It then departs only slightly from the rawinsonde by as much as 15% RH between 225 m and 425 m in height. Another 20% disparity occurs between

775 m and 875 m in height. The 9-km COAMPS® profile has the humidity gradient captured well up to 215 m but is off by more than 10% near the surface and less above 140 m. The 3-km and 9-km COAMPS® profiles on the 9th are reasonably accurate for the humidity gradients up to roughly the 450-m level. The 3-km COAMPS® profile caught the decrease in RH just before the rapid drop at the 200-m level, but the 9-km resolution did not. All COAMPS® gradients for the 2335 UTC plot are in agreement up to approximately 140 m in height.

Relative humidity RMS differences from interpolated soundings for each sigma level were between 3.96 and 40.74% for the 9-km COAMPS® runs. The maximum RMS difference occurred at the 330-m sigma level. This matches exactly with the 9-km COAMPS® maximum RMS temperature difference. RMS differences for the 3-km COAMPS® runs were between 4.02 and 42.13%, with the maximum occurring at the 215-m sigma level. These RMS ranges show no significant improvement in predicted RH values from the 9-km to 3-km resolutions.

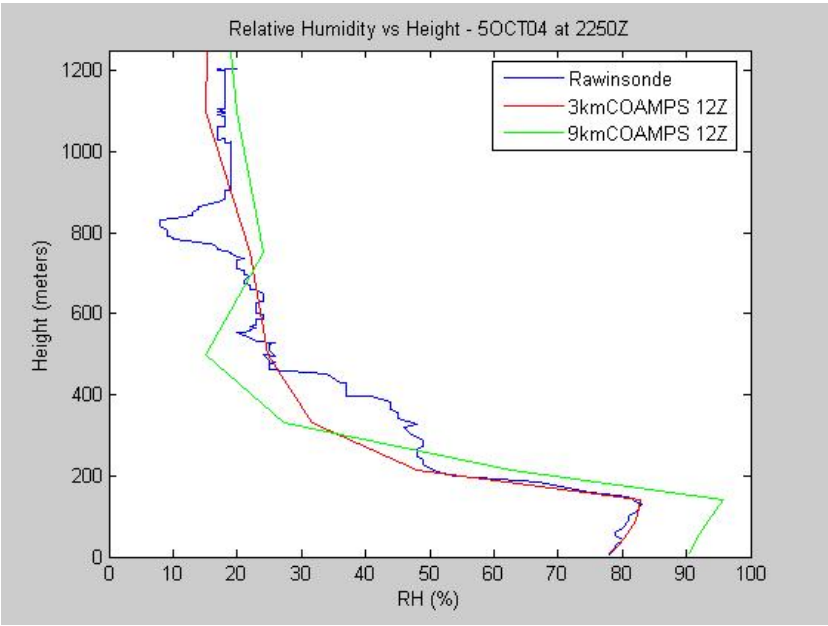

Fig. 19. Relative humidity (in %) vs. height (in meters) for COAMPS® 9-km and 3-km interpolations and October 5th at 2250 UTC rawinsonde.

The vertical resolution of the rawinsondes in conjunction with the launching process prohibits accurate identification of the evaporation duct. However, it should be noted they identified drops in RH from the surface value in nine instances, which would have signified a possible evaporation duct. Possible evaporation duct identifications from rawinsondes occurred on all October 6th soundings except for 1042 and 1508 UTC, October 7th at 1148 UTC, October 8th at 0251 and 2324 UTC, and both soundings on October 9th. Of those listed, Fig. 20 shows the 2335 UTC sounding of RH for October 9th. Neither the 9-km nor the 3-km COAMPS® runs predicted any evaporation ducts.

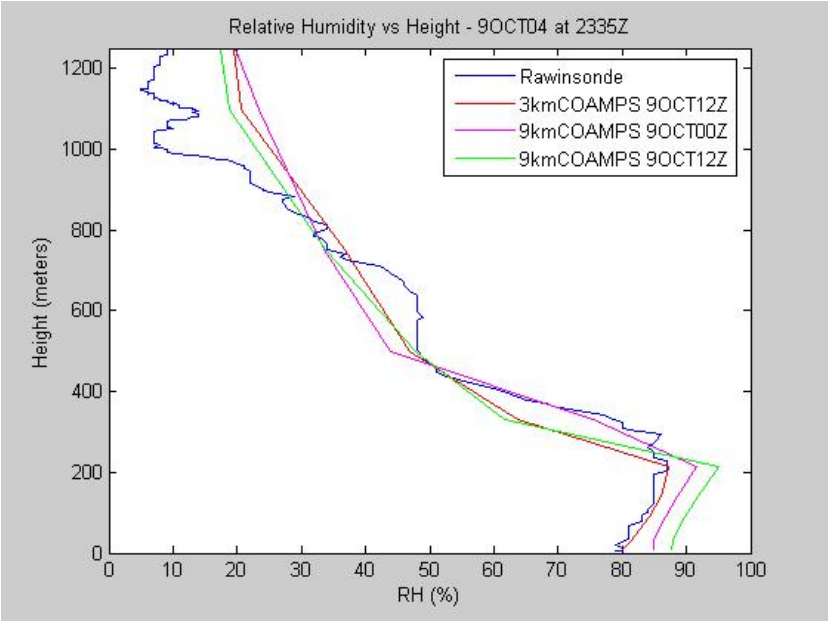

Fig. 20. Relative humidity (in %) vs. height (in meters) for COAMPS® 9-km and 3-km interpolations and October 9th 2335 UTC rawinsonde.

d. Modified Refractivity

Figure 21 is a time-arranged display of M profiles from all rawinsondes launched during SILENT HAMMER. It provides a good summary of the significant variation of the ducting conditions over those five days. Of note are the last eight M profiles in the series. The time sequence of profiles show a transition from elevated ducts, for the 5th through 7th of October, to surface-based ducts on the 8th. The final two profiles on the 9th show an almost standard atmosphere. Numerically there was an elevated duct

present in each of the last two rawinsondes, but they were both relatively shallow and extremely weak. The transition from surface-based ducts to weak elevated ducts corresponds to the cold front that passed through the area around 1800 UTC on the 9th of October mentioned earlier.

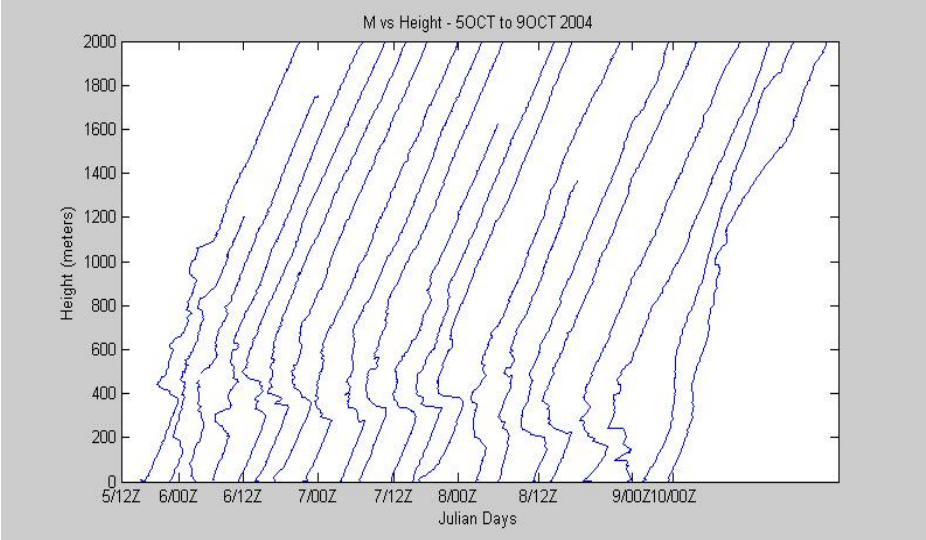

Fig. 21. Rawinsonde M profiles for 5 to 9 OCT 2004.

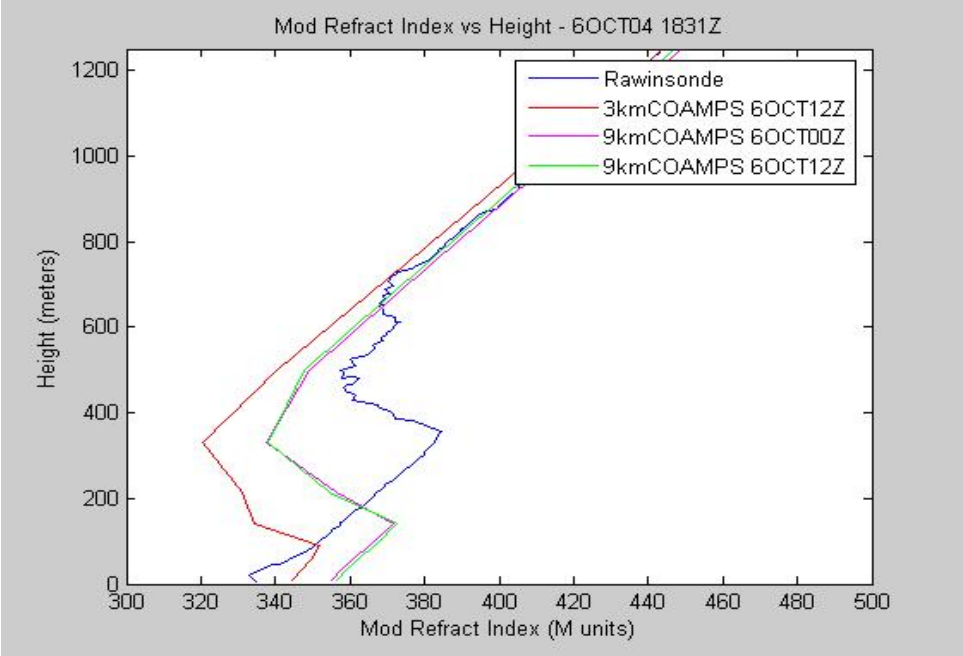

Fig. 22. M values vs. height (in meters) for COAMPS® 9-km and 3-km interpolations and October 6th 1831 UTC rawinsonde.

Calculating M from COAMPS® input variables and assuming the rawinsonde soundings to be ground truth, Figure 22 shows one case when COAMPS® did not predict M profiles well with regard to elevated ducts. Of the 15 elevated ducts observed in the rawinsonde profiles, the 9-km COAMPS® runs predicted only two. The 3-km COAMPS® forecasts were only slightly better with three of the 15 elevated ducts predicted. However, both COAMPS® resolutions did manage to qualitatively forecast all six surface-based ducts that occurred on the 8th of October. Figure 23 shows such a case where COAMPS® correctly forecasted a surface-based duct, although the attributes of the predicted duct are

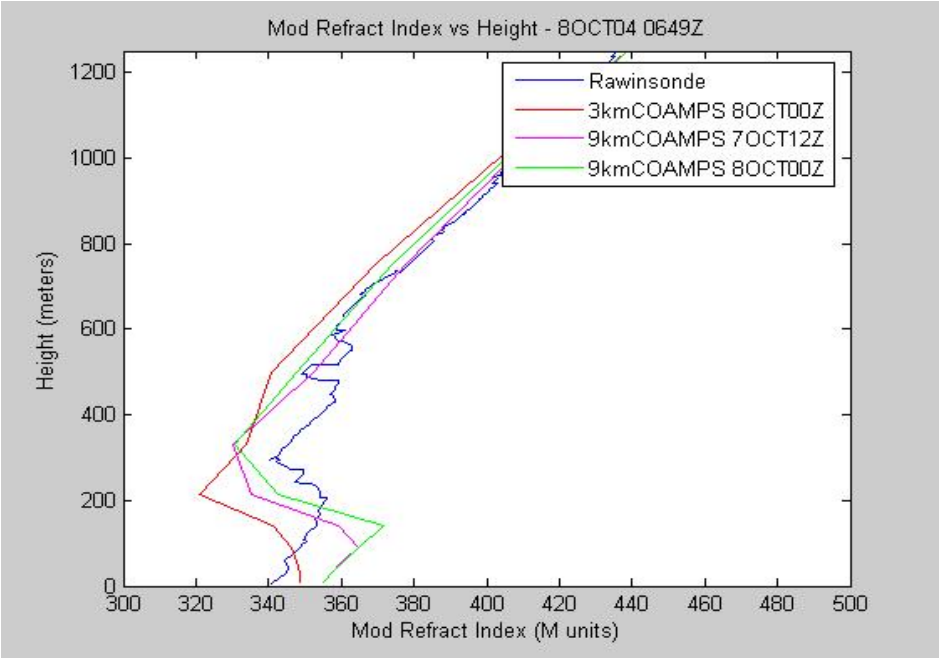

Fig. 23. M values vs. height (in meters) for COAMPS® 9-km and 3-km interpolations and October 8th 0649 UTC rawinsonde.

so different from what was observed that they will lead to very different propagation conditions. Both the 3- and 9-km COAMPS® falsely predicted surface-based ducts twelve times when the rawinsonde actually observed elevated ducts. In one instance, the 9-km COAMPS® falsely predicted there was no duct present when the rawinsonde indicated an

elevated duct. For the 9th of October, the weak elevated duct observed by the 1850 UTC rawinsonde was captured by the 3-km COAMPS® forecast but not the 9-km COAMPS® forecast. Both interpolations from COAMPS® forecasts predicted the weak elevated duct at 2335 UTC. Qualitatively, 9-km COAMPS® correctly forecasted the actual duct type observed by the rawinsondes only eight times out of 21 soundings, and the 3-km COAMPS® correctly predicted only nine out of the 21 duct types. Table 2 summarizes the general ducting predictions by both COAMPS® resolutions. To determine when COAMPS® predicted the correct duct type, look at Table 2 under the Observed column for the desired duct type. The numbers along the diagonals, i.e. surface-based Observed and surface-based COAMPS, should equal the number in the total column. There should be zeroes in the remaining columns of that row. To determine when COAMPS® predicted the incorrect duct type, look at numbers off the diagonals where the Observed does not match the COAMPS® column duct type.

Table 2. Duct predictability of 9-km and 3-km COAMPS® for October 5th through 9th of 2004 off San Clemente Island.

	9-km COAMPS®				3-km COAMPS®			
Observed	Sfc-based	Elev	None	Total	Sfc-based	Elev	None	Total
Sfc-based	6	0	0	6	6	0	0	6
Elev	12	2	1	15	12	3	0	15
Total	18	2	1	21	18	3	0	21

RMS errors for M values were between 5.46 and 32.51 M units for the 9 km COAMPS® forecasts. RMS errors for the 3-km COAMPS® forecasts were between 4.70 and 37.88 M units. These number ranges show that the 3-km COAMPS® forecasts do not significantly improve M calculations over the 9-km COAMPS® forecasts. It should be pointed out that the 9-km RMS errors were less than the 3-km RMS errors at the 140-m, 215-m and 330-m sigma levels. Appendix A contains all M profiles.

More important to the study of ducting effects are the errors in height between the rawinsonde profiles and COAMPS® profiles for significant M locations. Referring again to Figure 4, the height of M_{max} is important since it is the beginning of the trapping layer. Similarly M_{min} is also important since it is the top of the trapping

layer, and hence the top of the duct, and also helps determine numerically if a duct is surface-based or elevated.

After calculating RMS errors in M for each COAMPS® sigma level, the rawinsonde and COAMPS® heights for M_{max} and M_{min} were compared along with the duct strengths and heights. Duct strength is simply the change in M from M_{max} to M_{min} divided by the trapping layer depth. Tables 3 and 4 summarize the errors associated with M and their corresponding duct parameters. The 9-km COAMPS® predicted M_{max} more correctly than the 3-km COAMPS®, but the 3-km was better at M_{min}. The 3-km COAMPS® forecasts were also better at predicting the difference between M_{min} and M_{max} (Delta M in Table 4) showing improved performance within the trapping layer. Both sets of COAMPS® data were nearly equal at predicting M_{excess}, i.e. the difference between M_{min} and the M value nearest the surface. The RMS error for trapping layer base height was 162.01 m for the 9-km COAMPS® runs and 212.95 m for the 3-km COAMPS® runs. The RMS errors for the trapping layer depth were very close for both the 9-km and 3-km COAMPS® runs at 130.35 m and 132.78 m, respectively. The RMS errors for the overall duct height (the height of M_{min}) were 129.1 m for the 9-km COAMPS® run and 117.1 m for the 3-km COAMPS® run. The errors in duct strength between the rawinsondes and COAMPS® were also close at 4.45 M units m^{-1} for the 9-km and 4.35 M units m^{-1} for the 3-km COAMPS® runs. The closeness of RMS errors in trapping layer depth, duct height and duct strength are perhaps due in part to the sigma levels for the 9-km and 3-km COAMPS® runs being the same. However, this reasoning would also suggest that the RMS error for trapping layer base height would be small as well, and it is not.

Looking at the specific values for duct heights, all but one of the 9-km runs predicted 330 m with one value at 500 m. The 3-km COAMPS® run varied more with nine predictions at 330 m, nine predictions at 215 m, two predictions at 140 m, and one at 500 m. Also noteworthy were the trends associated with trapping layer base heights and overall duct heights. All trapping layer base height differences between the rawinsondes and COAMPS® runs were positive. This means the normal and high-resolution COAMPS® forecasts predicted trapping layer base heights that were too low. This follows the results found by Wash et al. (1998) when COAMPS® predicted the general structure of the mixed layer but predicted the depth too shallow. However, the

overall duct height differences were mixed. Ten of the 21 duct height differences between the rawinsonde and 9-km COAMPS® were negative. The 3-km COAMPS® forecasts over-predicted the duct heights three out of 21 times. Both positive and negative mean differences for the 3-km COAMPS® duct heights were less than the 9-km mean differences.

Table 3. Mean and RMS errors (in meters) for trapping layer base height and depth, duct base height and overall duct height.

	TL Base Ht (m)		TL Depth (m)		Duct Bs Ht (m)		Duct Ht (m)	
	Mean	RMS	Mean	RMS	Mean	RMS	Mean	RMS
Sonde	273.24		84.67		138.81		357.7143	
9kmCOAMPS	129.76	162.01	190.24	130.35	119.46	109.74	322.381	129.0906
3kmCOAMPS	78.81	212.95	191.90	132.78	102.14	114.32	270.7143	117.1277

Table 4. Mean and RMS errors (in M units unless otherwise noted) for M_{max}, M_{min}, ASTD (Delta M), M_{excess} and duct strength.

	Mmax		Mmin		Delta M		Mexcess		Duct Strength (M units/m)	
	Mean	RMS	Mean	RMS	Mean	RMS	Mean	RMS	Mean	RMS
Sonde	369.37		346.64		22.74		9.00		1.38800	
9kmCOAMPS	351.12	12.59	331.19	23.79	32.92	19.00	-19.26	31.55	0.15924	4.45238
3kmCOAMPS	356.24	20.18	331.91	20.50	24.33	12.86	-17.38	30.00	0.17931	4.34563

B. COMPARISONS OF AREPS RESULTS WITH RADIOSONDE AND COAMPS® DATA INPUT

The following sections visually demonstrate the sensitivities of EM propagation to varying atmospheric conditions, and specifically the effect that the differences between the rawinsonde and COAMPS® M profiles will have on propagation. As stated previously, each rawinsonde was used within AREPS to create an environment file. These files were then used as inputs to run AREPS for the different assumed radar frequencies of 1, 3, 10, and 18 GHz and a transmitter height of 150 feet to make plots of

propagation loss (in dB) vs. height (in feet) and range (in NM). The rawinsonde-generated propagation losses were then compared with the 9-km and 3-km COAMPS®-generated propagation losses.

1. Radar Loss Results with Rawinsonde Input

Figure 24 shows propagation loss coverage diagrams for all four frequencies for the 1827 UTC rawinsonde launched on October 5th. In the following discussion we will

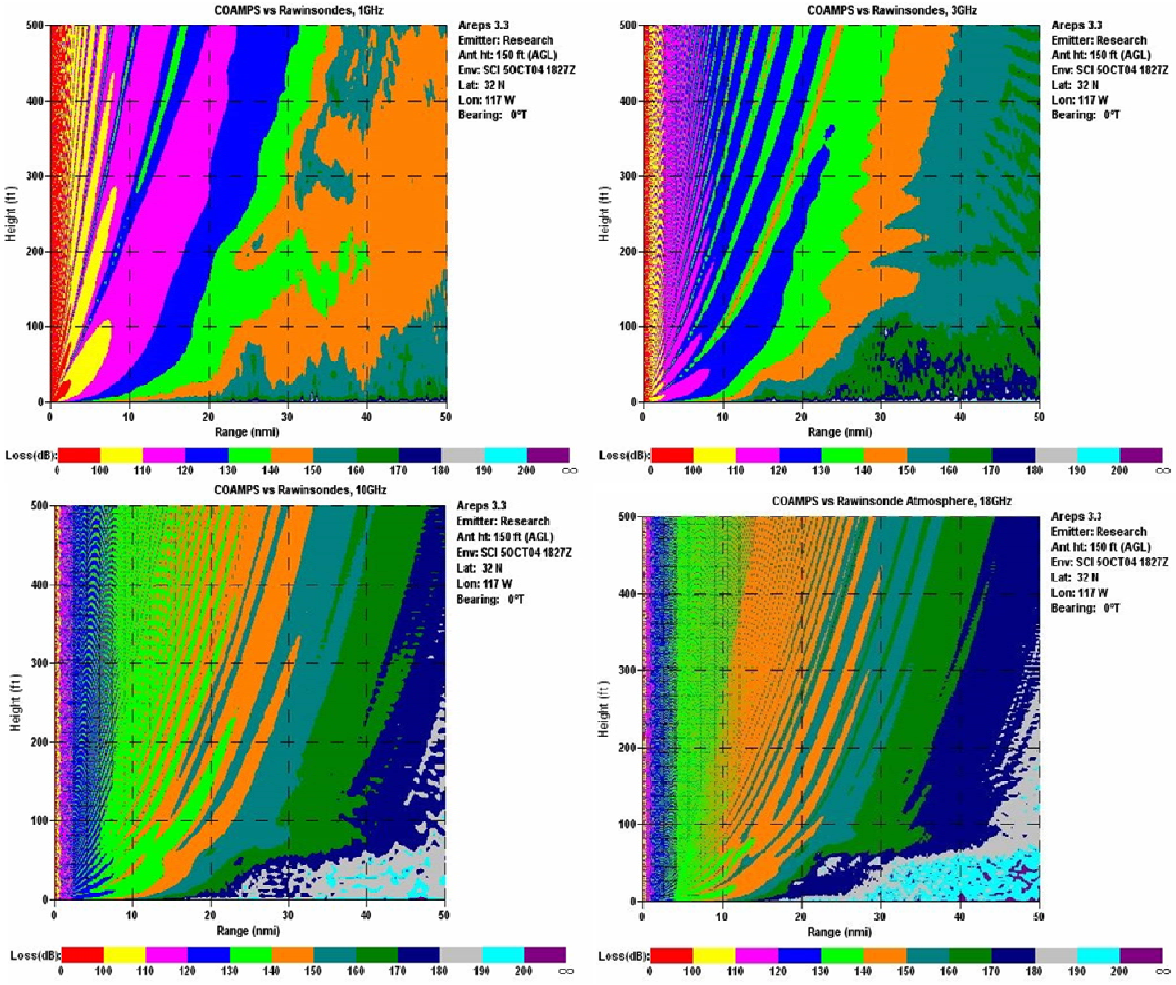

Fig. 24. Propagation loss (in dB) vs. height (in ft) and range (in NM) for 1 GHz (upper, left), 3 GHz (upper, right), 10 GHz (lower, left) and 18 GHz (lower, right) for rawinsonde on October 5th 2004 at 1827 UTC.

assume the radars are searching for a target at 100 feet and with a propagation loss threshold of 140 dB. Regions with a propagation loss greater than 140 dB indicate where the target cannot be detected. Regions less than 140 dB indicate where the target can be detected by radar. It is evident from the changing prop loss coverage diagrams that

detection range decreases significantly as frequency is increased from 1 to 18 GHz. At 1 GHz frequency and a height of 100 feet, the prop loss threshold value of 140 dB occurs at approximately 24 NM. The detection range for this same prop loss value for 3 GHz and 100 feet shortens to about 21 NM range. Increasing the frequency to 10 GHz decreases detection range again, to approximately 18 NM, and the final increase in frequency to 18 GHz decreases the horizontal range by half this amount (i.e. nine NM). Table 5 summarizes the results from AREPS for all rawinsonde environments. In such a case a small aircraft or target would have been detected from 50 NM in to the antenna transmitter.

Table 5. Propagation loss ranges (in NM) for rawinsonde environments (P represents a "pocket", or small horizontal and/or vertical area, of the 140-dB prop loss threshold. The * denotes when the coverage diagram suggests the range to a prop loss value of 140 dB is greater than 50 NM. N/A means there was no occurrence of the prop loss threshold value at 100 feet within the 50-NM coverage diagram).

Date	Time	130-140 dB Range (NM)			
	(UTC)	1 GHz	3 GHz	10 GHz	18 GHz
5-Oct-04	1827	24	21	18	9
	2250	41	50	16	13
6-Oct-04	0238	NA	50	31	18
	0621	NA	50	50	49
	1042	NA	50	49	14
	1508	49	50	16	11
	1831	NA	47	50	26
	2244	47	49*	50	13
7-Oct-04	0221	NA	50	45	P44
	0717	NA	50	40	P39
	1148	NA	50	P46	12
	1458	43	50	P47	12
	1901	24	23	21	12
8-Oct-04	0251	NA	50	49	P45
	0649	NA	49	P47	P45
	1058	NA	50	P45	P39
	1510	NA	50	P47	P34
	1933	P38	50	P49	P32
	2324	NA	50	P49	P35
9-Oct-04	1850	25	24	17	12
	2335	25	23	P20	12

2. AREPS Comparisons with 9-km COAMPS® Input Data

After calculating prop loss vs. range and height for the rawinsonde environments, the COAMPS® predicted profiles at 9-km and 3-km resolution were input to AREPS with the same transmitter height and frequencies. Figure 25 shows the four transmitter

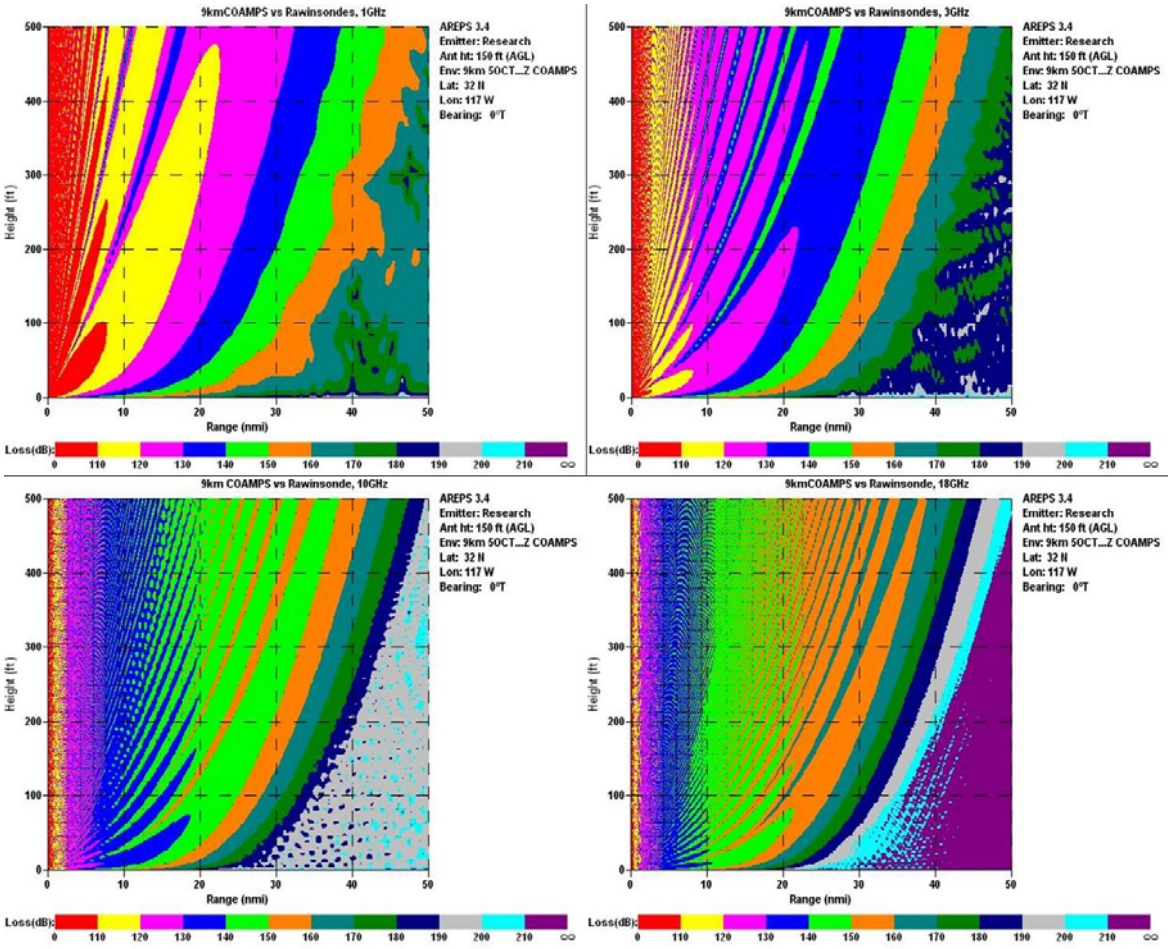

Fig. 25. Propagation loss (in dB) vs height (in ft) and range (in NM) for 1 GHz (upper left), 3 GHz (upper right), 10 GHz (lower left), and 18 GHz (lower right) on October 5th at 1827 UTC for 9-km COAMPS® environmental profile.

frequencies for the same date and time as Figure 24 (October 5th at 1827 UTC) for the 9-km COAMPS® predicted profiles. Although the rawinsonde M profiles differed from the COAMPS® predicted M profiles sporadically in height and absolute M values (discussed above in Section III, A.2), rawinsonde prop loss diagrams agreed surprisingly well with the 9-km COAMPS® predicted prop loss diagrams. Table 6 summarizes the 9-km COAMPS® predicted detection ranges for a 100 foot target and a prop loss threshold

value of 140 dB. Tables 7 and 8 show the differences, in percentage and nautical miles respectively, between the rawinsondes and 9-km COAMPS® ranges for the same prop loss detection value. There were 21 rawinsonde launches from the R/S Acoustic Explorer, with corresponding COAMPS® profiles for the 9-km and 3-km resolution, and four frequency plots for each one. This totals to 84 potential range differences between a

Table 6. Propagation loss ranges (in NM) for 9-km COAMPS® environments.

Date	Time (UTC)	Range (in NM) to 140 dB Prop Loss 1 GHz	3 GHz	10 GHz	18 GHz
5-Oct-04	1827	25	23	16	9
	2250	50	23*	16	9
6-Oct-04	0238	31	49*	P47	9
	0621	45	50*	17	9
	1042	47	50*	P49	10
	1508	47	50*	P50	9
	1831	46	50*	16	9
	2244	32	49*	P47	10
7-Oct-04	0221	P40	50*	P45	9
	0717	47	50*	16	9
	1148	36	50*	P48	9
	1458	43	50*	16	10
	1901	50	23*	16	9
8-Oct-04	0251	NA	50*	P50	9
	0649	34	50*	P46	9
	1058	NA	50*	32	9
	1510	43	50*	P48	9
	1933	P42	50*	P47	9
	2324	31	50*	P48	9
9-Oct-04	1850	26	24	18	9
	2335	26	25	17	8

rawinsonde profile and each of the COAMPS® profiles. The 9-km resolution COAMPS® had 74 measurable range differences, of which 22 did not change at all. This means the COAMPS®-generated coverage diagram from AREPS predicted 22 times what the rawinsonde-generated coverage diagram also predicted. Of the remaining 52 differences, 16 were positive and 36 were negative. The simple mean of these 52 differences was -5.77 NM while the RMS difference was 15.02 NM. For the positive changes (i.e. an increase from the rawinsonde range to 9-km COAMPS® range), twelve differences were

between one and five NM. The four largest differences were nine, 16, 26 and 34 NM. The nine NM difference occurred on October 5th at 2250 UTC. The 16 and 34 NM differences occurred on October 6th at 0238 and 1508 UTC, respectively. The 26-NM difference occurred on the 7th of October at 1901 UTC. Interestingly, there were no positive differences in range for the 18-GHz runs. There were also no large range differences (i.e. greater than four NM) for the 8th or 9th of October, when the ducting situation had changed from surface-based to weakly elevated.

Table 7. Percent differences from rawinsonde propagation loss range to 9-km COAMPS® propagation loss range.

Date	Time (UTC)	% Difference from Rawinsonde to 9-km COAMPS® 140-dB Prop Loss			
		1 GHz	3 GHz	10 GHz	18 GHz
5-Oct-04	1827	4.17	9.52	-11.11	0.00
	2250	21.95	-54.00	0.00	-30.77
6-Oct-04	0238	(NA)	-2.00	51.61	-50.00
	0621	(NA)	0.00	-66.00	-81.63
	1042	(NA)	0.00	0.00	-28.57
	1508	-4.08	0.00	212.50	-18.18
	1831	(NA)	6.38	-68.00	-65.38
	2244	-31.91	0.00	-6.00	-23.08
7-Oct-04	0221	(NA)	0.00	0.00	-79.55
	0717	(NA)	0.00	-60.00	-76.92
	1148	(NA)	0.00	4.35	-25.00
	1458	0.00	0.00	-65.96	-16.67
	1901	108.33	0.00	-23.81	-25.00
8-Oct-04	0251	0.00	0.00	2.04	-80.00
	0649	(NA)	2.04	-2.13	-80.00
	1058	0.00	0.00	-28.89	-76.92
	1510	(NA)	0.00	2.13	-73.53
	1933	10.53	0.00	-4.08	-71.88
	2324	(NA)	0.00	-2.04	-74.29
9-Oct-04	1850	4.00	0.00	5.88	-25.00
	2335	4.00	8.70	-15.00	-33.33

For the 36 negative differences in range, half were between one and five NM. There was only one difference between six and 10 NM, two between 11 and 15 NM, one difference between 16 and 20 NM, and the remaining 14 range differences greater than 20 NM. All but one run of the 18-GHz frequency at 9-km resolution had a negative difference. The October 5th run at 1827 UTC for 18 GHz had no change. The 1- and 3-

GHz runs only had two negative changes each. Generally the 10- and 18-GHz runs were dominated by negative differences in range while the 1- and 3-GHz runs were dominated by positive range differences. For the 8th of October, when the general ducting situation changed from elevated to surface-based, most of the negative range variances were quite large. All but four were greater than 23 NM, one was 13 NM, and the remaining three were two NM or less.

Table 8. Propagation loss range differences (in NM) from rawinsonde profiles to 9-km COAMPS® profiles.

Date	Time (UTC)	Range Difference from Rawinsonde to 9-km COAMPS® 140-dB Prop Loss 1 GHz	3 GHz	10 GHz	18 GHz
5-Oct-04	1827	1	2	-2	0
	2250	9	-27	0	-4
6-Oct-04	0238	(NA)	-1	16	-9
	0621	(NA)	0	-33	-40
	1042	(NA)	0	0	-4
	1508	-2	0	34	-2
	1831	(NA)	3	-34	-17
	2244	-15	0	-3	-3
7-Oct-04	0221	(NA)	0	0	-35
	0717	(NA)	0	-24	-30
	1148	(NA)	0	2	-3
	1458	0	0	-31	-2
	1901	26	0	-5	-3
8-Oct-04	0251	0	0	1	-36
	0649	(NA)	1	-1	-36
	1058	0	0	-13	-30
	1510	(NA)	0	1	-25
	1933	4	0	-2	-23
	2324	(NA)	0	-1	-26
9-Oct-04	1850	1	0	1	-3
	2335	1	2	-3	-4

3. AREPS Comparisons with 3-km COAMPS® Input Data

Finally, environmental profiles for the 3-km COAMPS® resolution were input to AREPS to generate prop loss diagrams similar to the 9-km COAMPS® and rawinsonde environments already described. Figure 26 shows prop loss versus height and range for October 5th at 1827 UTC. Table 9 summarizes all detection ranges for all frequencies at

3-km resolution. Tables 10 and 11 present differences, in percentage and range respectively, between the rawinsondes and 3-km COAMPS® environments.

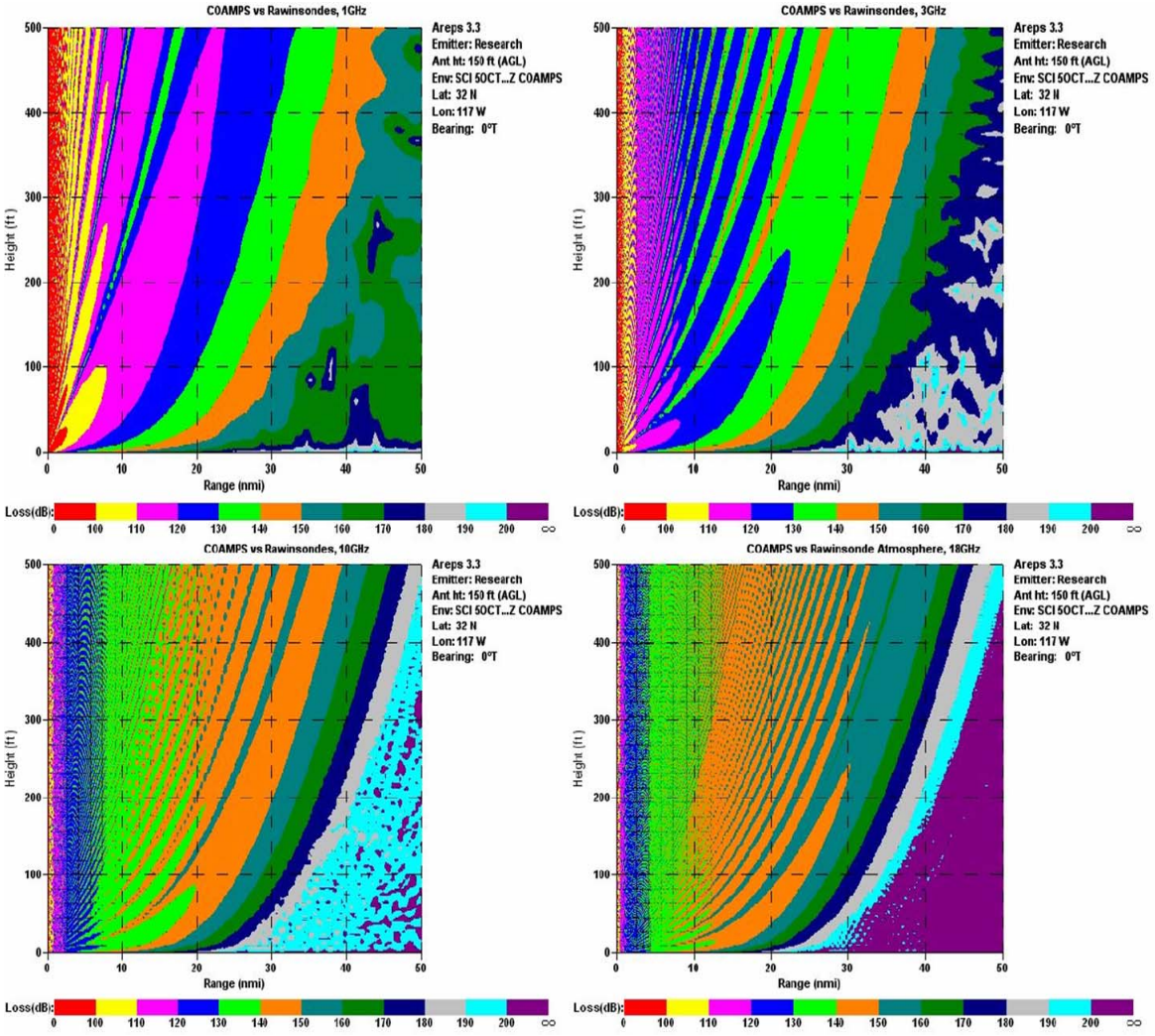

Fig. 26. Propagation loss (in dB) vs. height (in ft) and range (in NM) for 1 GHz (upper, left), 3 GHz (upper, right), 10 GHz (lower, left) and 18 GHz (lower, right) on October 5th 2004 at 1827 UTC for 3-km COAMPS® environmental profile.

For the changes in range, there were 82 measurable differences. The 3-km resolution made a drastic improvement over the 9-km resolution. Of the 82 differences that were measurable, 59 instances showed no change at all. No change in range means the COAMPS®-generated prop loss diagram correctly matched the rawinsonde-generated

Table 9. Propagation loss ranges (in NM) for 3-km COAMPS® environments.

Date	Time (UTC)	Range (in NM) to 140-dB Prop Loss 1 GHz	3 GHz	10 GHz	18 GHz
5-Oct-04	1827	25	24	P17	12
	2250	42	50	P21	12
6-Oct-04	0238	43	50	P46	13
	0621	NA	50	50	P49
	1042	P40	50	P49	13
	1508	P49	50	17	12
	1831	NA	50	50	P26
	2244	47	49*	50	13
7-Oct-04	0221	NA	50	P45	P45
	0717	NA	50	P40	P39
	1148	NA	50	P46	12
	1458	P42	50	P19	12
	1901	24	22	P20	12
8-Oct-04	0251	NA	50	P47	P41
	0649	NA	49*	P46	P45
	1058	NA	50	P45	P39
	1510	NA	50	P47	P34
	1933	P38	50	50	P32
	2324	NA	50	49	P40
9-Oct-04	1850	25	24	P17	12
	2335	25	23	P20	12

prop loss diagram. Numerically, there were 11 negative and 12 positive changes. For the positive range changes, all but one were between one and five NM. The largest was 15 NM that occurred on October 6th at 0238 UTC for 10 GHz. The negative range differences paralleled the positive with all but one between one and five NM. The largest negative range difference was -28 NM that occurred on October 7th at 1458 UTC. This largest difference also happened for the 10-GHz run. The simple mean difference was 0.32 NM with an RMS difference of 3.74 NM. There was no discernible pattern change in prop loss for the 8th of October when the general ducting situation transformed from an elevated to a surface-based environment.

Table 10. Percent differences from rawinsonde propagation loss range to 3-km COAMPS® propagation loss range.

Date	Time (UTC)	% Difference from Rawinsonde to 3-km COAMPS® 140-dB Prop Loss			
		1 GHz	3 GHz	10 GHz	18 GHz
5-Oct-04	1827	4.17	14.29	-5.56	33.33
	2250	2.44	0.00	31.25	-7.69
6-Oct-04	0238	(NA)	0.00	48.39	-27.78
	0621	0.00	0.00	0.00	0.00
	1042	(NA)	0.00	0.00	-7.14
	1508	0.00	0.00	6.25	9.09
	1831	0.00	6.38	0.00	0.00
	2244	0.00	0.00	0.00	0.00
7-Oct-04	0221	0.00	0.00	0.00	2.27
	0717	0.00	0.00	0.00	0.00
	1148	0.00	0.00	0.00	0.00
	1458	-2.33	0.00	-59.57	0.00
	1901	0.00	-4.35	-4.76	0.00
8-Oct-04	0251	0.00	0.00	-4.08	-8.89
	0649	0.00	0.00	-2.13	0.00
	1058	0.00	0.00	0.00	0.00
	1510	0.00	0.00	0.00	0.00
	1933	0.00	0.00	2.04	0.00
	2324	0.00	0.00	0.00	14.29
9-Oct-04	1850	0.00	0.00	0.00	0.00
	2335	0.00	0.00	0.00	0.00

Since these data sets are from early October, Daylight Savings Time had not been initiated. This means there was a seven hour difference between UTC and Pacific Standard Time. The two largest range differences, therefore, took place at 1938 and 0758 local time. Sunset and sunrise for these days were at 1828 LT on the 5th and 0647 LT on the 7th of October, respectively. This shows the largest range differences occurred within roughly an hour and ten minutes of sunrise or sunset.

Table 11. Propagation loss range differences (in NM) from rawinsonde profiles to 3-km COAMPS® profiles.

Date	Time (UTC)	Range Difference from Rawinsonde to 3-km COAMPS® 140-dB Prop Loss 1 GHz	3 GHz	10 GHz	18 GHz
5-Oct-04	1827	1	3	-1	3
	2250	1	0	5	-1
6-Oct-04	0238	(NA)	0	15	-5
	0621	0	0	0	0
	1042	(NA)	0	0	-1
	1508	0	0	1	1
	1831	0	3	0	0
	2244	0	0	0	0
7-Oct-04	0221	0	0	0	1
	0717	0	0	0	0
	1148	0	0	0	0
	1458	-1	0	-28	0
	1901	0	-1	-1	0
8-Oct-04	0251	0	0	-2	-4
	0649	0	0	-1	0
	1058	0	0	0	0
	1510	0	0	0	0
	1933	0	0	1	0
	2324	0	0	0	5
9-Oct-04	1850	0	0	0	0
	2335	0	0	0	0

C. *BUILDER*™ COMPARISONS

1. *Builder* Results with Rawinsonde Input Data

One difficulty with the current version of *Builder* is its inability to input elevated ducts into the METOC effects section. It does, however, let the user input surface-based duct information and surface duct (i.e. the evaporation duct) information. This information is limited to single values for air temperature, surface wind, absolute humidity, and duct height and strength. Individual meteorological values at different profile levels are not currently part of the *Builder* input process. This limits analysis to the 8th of October when the general ducting environment was dominated by surface-based ducts.

When choosing the duct strength, the user can only be subjective. *Builder* options for duct strength are none, weak, normal, strong, and extreme. Users are left to determine themselves which choice to make. The next version of the Interactive Scenario *Builder*

will incorporate more options for meteorological effects by allowing the user to download U.S. Navy (through FNMOC) or U.S. Air Force (through the Air Force Weather Agency) weather model data.

It is difficult to compare AREPS results, provided as one-way prop loss, with *Builder* results which are provided as signal-to-noise ratio (SNR), signal strength or probability of detection (P_d). For the purposes of continuing the sensitivity study, we will assess the signal-to-noise ratios between the different EM models. Figure 27 is an SNR plot from *Builder* for a surface-based duct sounding on October 8th at 1933 UTC using the MMWave model for all four assumed radar transmitter frequencies. Like the

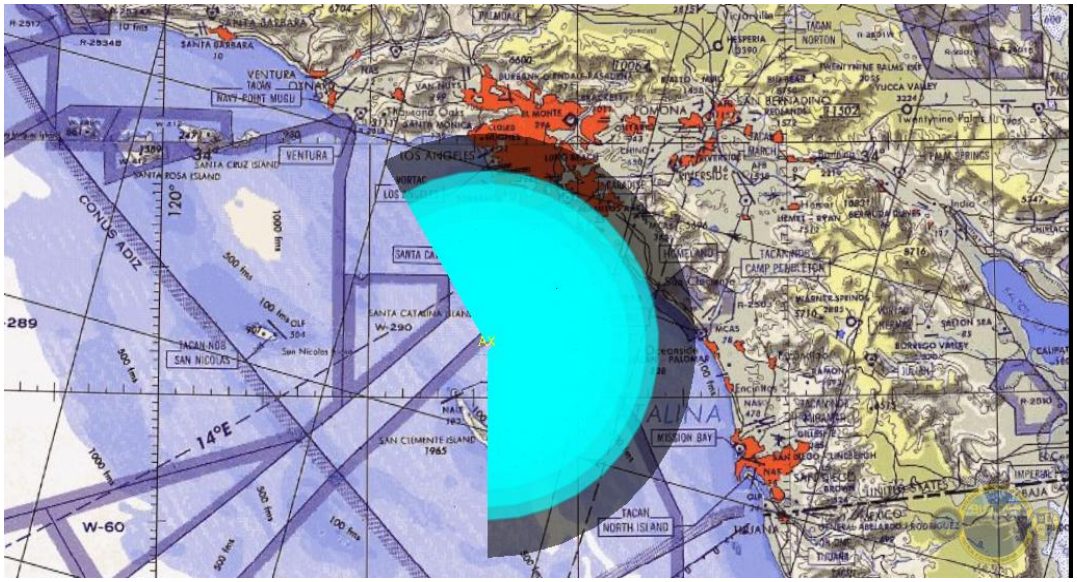

Fig. 27. *Builder* signal-to-noise ratio plot using the MMWave model for October 8th at 1933 UTC at 1, 3, 10 and 18 GHz.

coverage diagrams generated by AREPS, meteorological values were input to the program for four transmitter frequencies. These METOC descriptions were then used by *Builder* within the different EM propagation models to graph SNR versus range. After generating the SNR plot for all models at the four different frequencies, the Plot Analysis option was utilized to find the exact SNR value at 100 feet and 10-NM range. All SNR values for the rawinsonde meteorological inputs were positive. The duct height from the 1933 UTC rawinsonde, as measured by the height of M_{min}, was 280 m. One lesson

learned by this application of *Builder* was to use a smaller margin between the maximum discernible SNR and ideal SNR, which are both selectable in the Scenario Editor under the Actions window using the Edit Function command and Emissions tab. This will prevent SNR plots for four different frequencies appearing exactly the same and ease the confusion of the visual analysis brought on by similar diagrams (A. Goroch 2005, personal communication).

2. *Builder* Results with 9-km COAMPS® Input Data

Following the rawinsonde data input procedures for *Builder*, the 9-km COAMPS® meteorological values were used to define the ducting features. Figure 28 shows the MMWave output for the same date and time as Fig. 27. These dark colors in *Builder* correspond to a negative SNR, which means the signal strength at a point is less than the noise field strength. A positive SNR shows when the signal strength is greater than the noise field strength. The 9-km COAMPS run through *Builder* resulted in both positive and negative SNR values. Negative SNR values were isolated to the TIREM, MMWave and FFACTR models. The surface-based duct height for the 9-km COAMPS® was 330 m.

Fig. 28. *Builder* signal-to-noise ratio plot using the MMWave model for October 8th at 1933 UTC for 1, 3, 10 and 18 GHz.

3. *Builder* Results with 3-km COAMPS® Input Data

Finally, the 3-km COAMPS® environmental values were input to *Builder*. As before, the SNR plots were generated using four frequencies and then the actual SNR value at 10 NM and 100 feet was recorded. There were both positive and negative SNR values with the negative values isolated to the same models as before. Although specific SNR values were different, Figure 28 also represents the MMWave model results for the 3-km COAMPS® inputs. The 3-km COAMPS® profile for 1933 UTC predicted a duct height of 215 m.

Table 12 summarizes the SNR values for the six EM models and four transmitter frequencies. Even though the height of the 9-km COAMPS® surface-based duct was higher and the 3-km COAMPS® lower than that measured by the rawinsonde, both runs of COAMPS® had negative SNR values for the same EM models. The RMS differences for each of the individual EM models for the 3-km COAMPS® were all greater than the 9-km RMS differences with the exception of the Freespace model, which is the simplest model of all. Due to time constraints, the VTRPE model was not used but one could expect errors as much as 20% in propagation loss (Doggett, 1997).

Table 12. Signal-to-noise ratios calculated by different models within *Builder* at four transmitter frequencies.

Freq	*Builder* SNR's 8OCT 1933Z - Rawinsonde Environments					
(GHz)	Freespace	TIREM	MMWave	APM	RPO	FFACTR
1	108.49	89.66	108.49	90.59	89.37	90.56
3	99.11	88.63	98.35	88.55	87.66	87.95
10	87.74	85.48	87.74	85.23	85.02	85.31
18	80.89	79.84	79.62	82.20	81.91	83.20
	9-km COAMPS® Environments					
1	109.45	-27.75	-27.75	91.35	90.35	-27.75
3	99.31	-27.89	-27.89	89.38	89.35	-27.89
10	88.70	-28.50	-28.50	87.42	86.42	-28.50
18	82.65	-29.55	-29.55	83.08	82.24	-29.55
	3-km COAMPS® Environments					
1	108.45	-28.75	-28.75	89.35	88.31	-28.75
3	98.31	-28.89	-28.89	86.84	86.16	-28.89
10	87.70	-29.50	-29.50	83.79	82.78	-29.50
18	81.65	-30.55	-30.55	79.41	78.57	-30.55

D. NPS BULK MODEL COMPARISONS

1. Meteorological Data

Figures 29-33 show scatter plots of observed and COAMPS® predicted air temperature, relative humidity, and temperature difference values and evaporation duct height values calculated from observed and predicted data. They are plotted against the ship's measured values every three hours beginning at the 6-hr forecast. The predicted values are plotted along the y-axis against the measured values plotted along the x-axis. The x-axis values are direct measurements from the ship's data system (T_{air}, RH and SST) or calculations from the NPS bulk model using the ship's measurements. The 9-km COAMPS® predicted air values are in red and the 3-km values in blue. All 9-km COAMPS® RMS errors for air temperature, shown in Fig. 29, were lower than the 3-km COAMPS® errors with the exception of the 9-hr forecasts which were equal. At this time, there is no explanation for this variation from expectations.

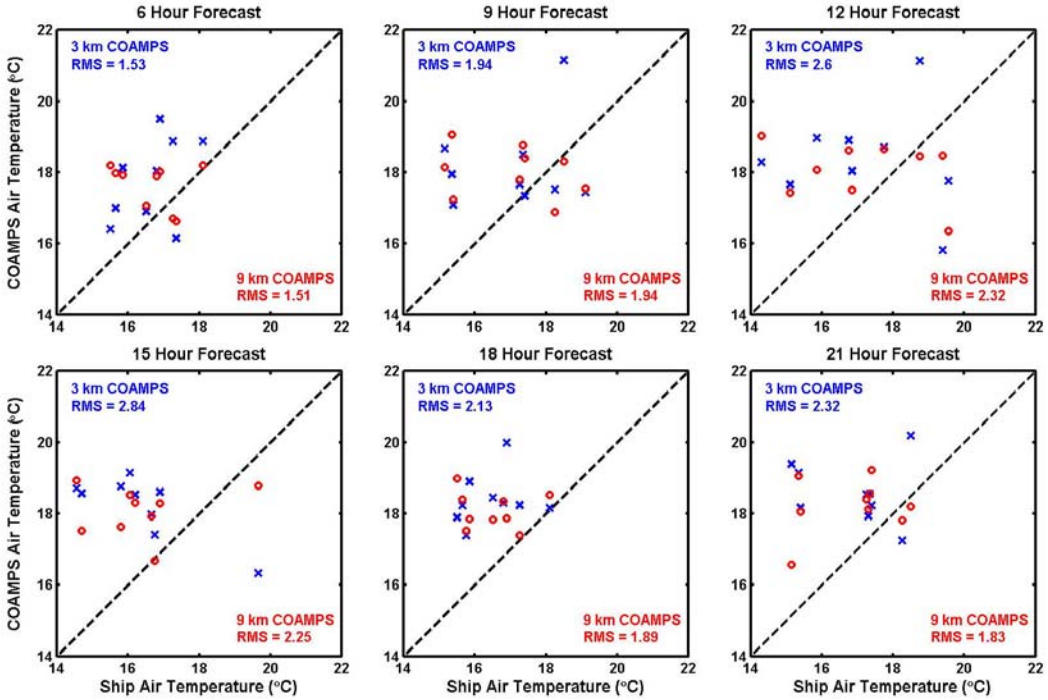

Fig. 29. Scatter plots of COAMPS® and ship air temperatures every three hours from the 6- to 21-hr forecasts.

Figure 30 shows the error between the SST used for COAMPS® and the ship's measured SST. Although labeled as "COAMPS® SST", this is not a true SST from

COAMPS®. Since the high-resolution COAMPS® data did not contain SST fields, we were unable to run the NPS bulk model using a true COAMPS® SST and COAMPS® air value. NAWC did not have these SST fields archived and had many prior operational commitments which precluded the re-running of the COAMPS® analysis and forecast fields. A 9-km COAMPS® model centered on Monterey Bay and including the San Clemente Island area, maintained by NRL Monterey, was planned to be used. However, the files for October of 2004 were archived at the Naval Oceanographic Office in Mississippi which was affected by Hurricane Katrina. Therefore, we used the MCSST sea temperatures which are an input to the NAWC COAMPS® model. They are a compilation of observations and not a forecast, but we felt they would be the closest we could obtain. We were also curious as to their value for data fusion purposes, i.e. would combinations of different data sources be a viable alternative to *in-situ* measurements in the future. Obviously the MCSST temperatures were higher than the temperatures measured aboard the R/S Acoustic Explorer.

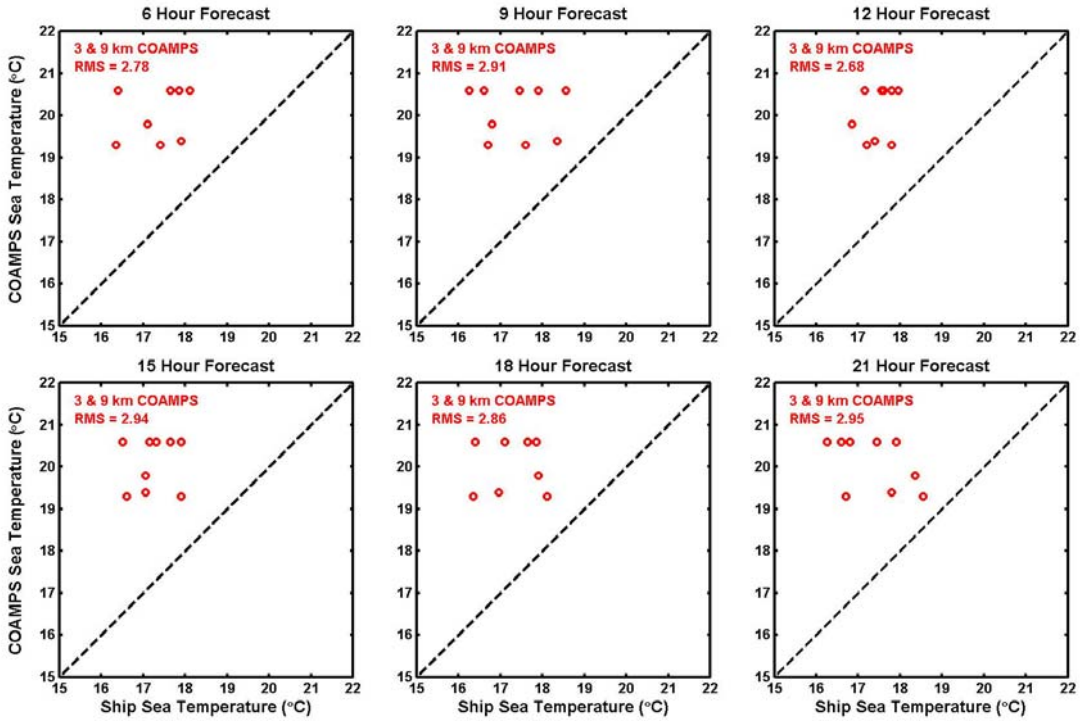

Fig. 30. Ship's measured SST versus input SST to COAMPS® model runs.

Figure 31 shows how the use of MCSST affected the temperature differences between air and sea. Notice that the RMS errors from Fig. 29 carry over into the RMS errors for ΔT in Figure 31. The air-sea temperature difference (ASTD) is important because it is a good indicator of how the NPS bulk model should perform for EDH calculations. When the air-sea temperature difference is positive, conditions are stable and the bulk model is not expected to perform as well as when the ASTD is negative (i.e. unstable conditions). In general, stable conditions lead to higher EDH values and cases where the EDH is undefined. From Fig. 30 we can see that when the COAMPS® air temperature is used with the ship sea temperature, the ASTD is biased high as compared to the ship data. On the other hand, the COAMPS® air temperatures combined with the MCSST sea temperature produce ASTD values biased low. This difference is important and will be discussed in the next section.

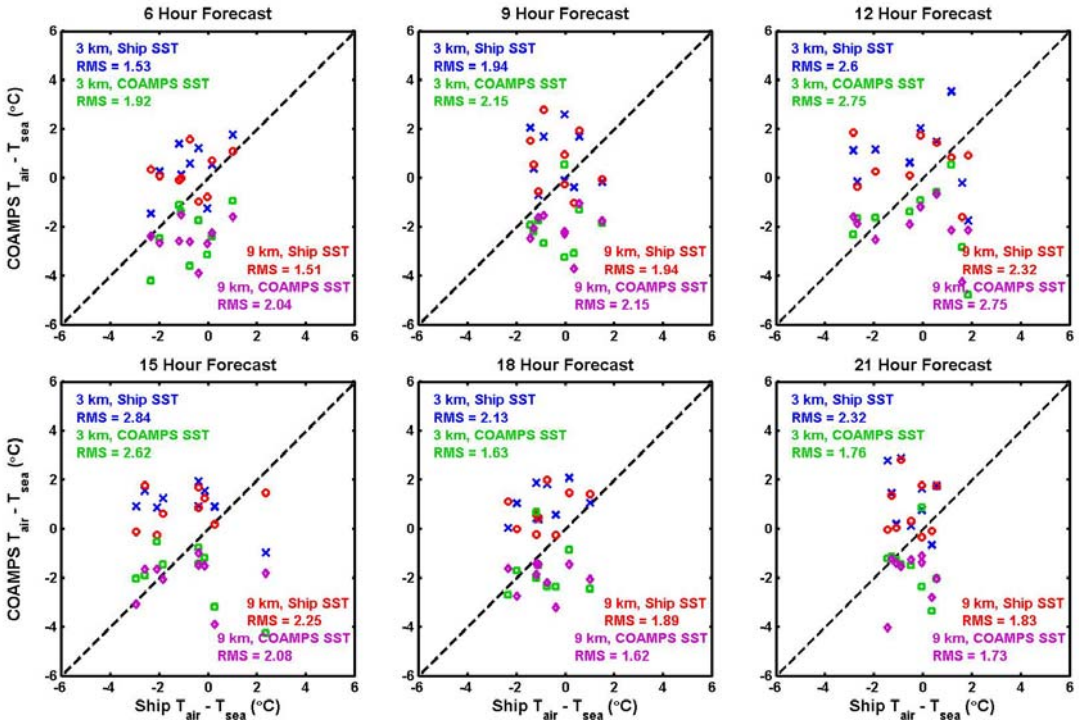

Fig. 31. Air-Sea Temperature Difference (T_{air} – SST) for data combinations of 3-km and 9-km COAMPS® with MCSST and ship's measured SST.

The relative humidity scatter plots, shown in Figure 32, reveal a slightly different result. The 3-km COAMPS® errors are lower at the 6- and 9-hr forecasts while the 9-km COAMPS® values have an equal or lower RMS difference for the remaining forecasts.

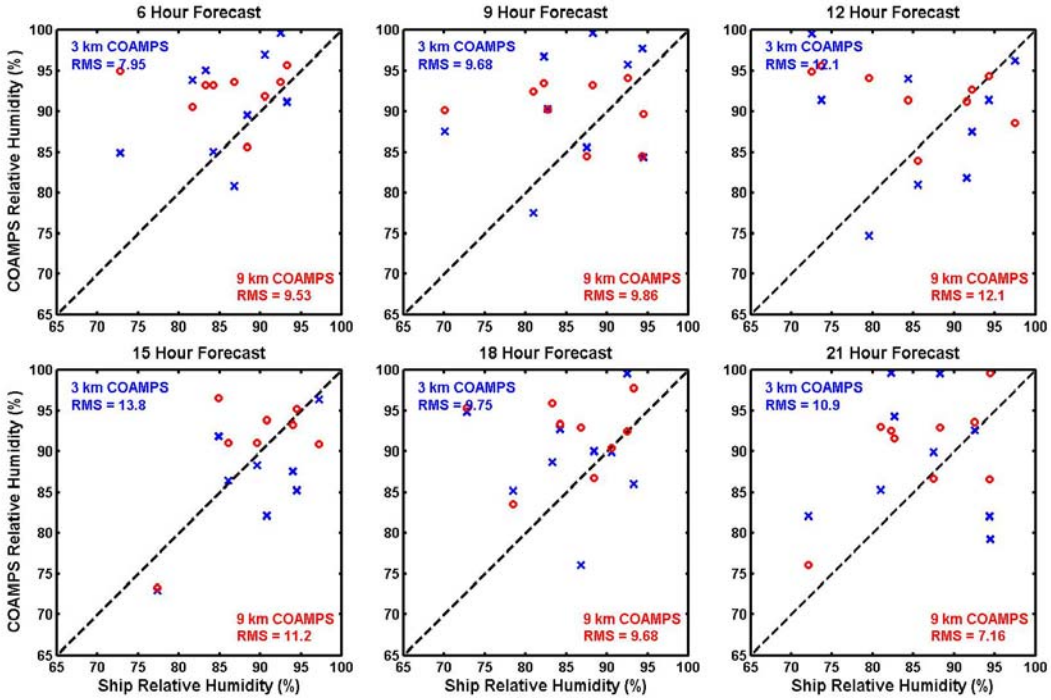

Fig. 32. Scatter plots of COAMPS® relative humidity every three hours from the 6- to 21-hr forecasts.

Figure 33 shows the variability of the evaporation duct height computed from both the 3-km and 9-km COAMPS® data using the NPS bulk model. Here the calculations using the ship's data within the NPS bulk model are considered ground truth since bulk models have shown good results in the past, at least in unstable conditions. Some examples are Hitney (2002), Babin and Dockery (2001), Frederickson et al. (1999) and Davidson et al. (1981).

The COAMPS® EDH values, shown Fig. 33, were computed two separate ways. First, the COAMPS® atmospheric data were combined with MCSST sea temperature values to calculate evaporation duct heights. Secondly, the COAMPS® atmospheric data were combined with the ship's *in-situ* sea temperature. This was done to examine whether having *in-situ* sea temperature data would improve the COAMPS® predictions,

in light of the fact that COAMPS® uses a constant sea temperature value throughout its forecast runs. The 9-km COAMPS® air values are combined with the ship's IR-measured SST (in red) and COAMPS® input SST (in purple). The 3-km COAMPS® air values are paired with the ship's SST (in blue) and model input SST (in green).

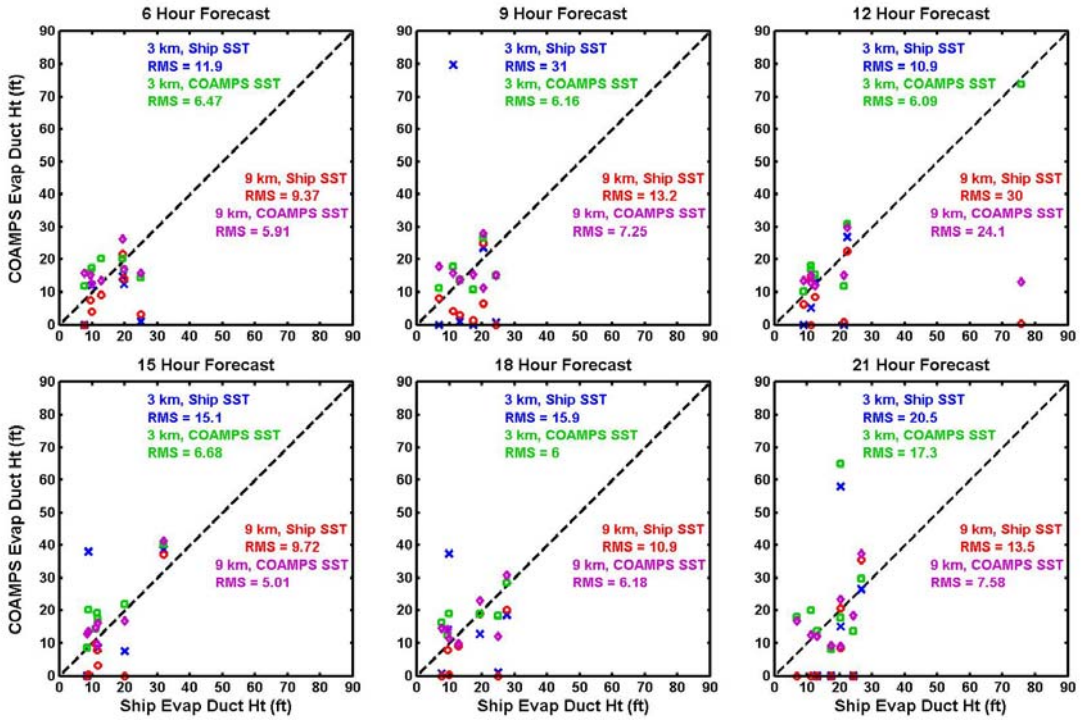

Fig. 33. Scatter plots of COAMPS® calculated evaporation duct heights every three hours from the 6- to 21-hr forecasts.

In every case the COAMPS® EDH values calculated with the MCSST sea temperature data agreed better the *in-situ* ship-derived EDH values than the COAMPS® data combined with the ship sea surface temperature values. This is due to the fact that, as mentioned above, the EDH calculations are very sensitive to the air-sea temperature difference. As seen previously in Figs 29-31, both the COAMPS® air and sea temperatures were biased high as compared to the ship data. This resulted in the all-COAMPS® ASTD agreeing better with the all-ship ASTD than when the COAMPS® air temperature was used with the ship sea surface temperature. The EDH values calculated with the COAMPS® atmospheric data and the ship sea temperature were therefore biased towards more positive ASTD conditions (i.e. stable conditions) where the NPS model

produces much higher values as compared to unstable conditions. It should be noted that Fig. 33 shows only those cases where the NPS evaporation duct model could return a solution. In some cases there was no EDH within the model's 50-m height domain, and therefore the EDH was considered to be undetermined. The 6-, 15- and 21-hr forecasts overall have the lowest RMS error from the combination of 9-km COAMPS® data and MCSST sea temperature. The remaining forecast times show that the 3-km COAMPS® and MCSST values are best. Curiously, the 12-hr forecasts show the calculations of evaporation duct using either sea temperature with the 3-km COAMPS® air predictions surpass the 9-km COAMPS® predictions. Also of note are the 21-hr errors. They show that both combinations of 9-km COAMPS® data are better than the 3-km COAMPS® data.

2. Propagation Model Determined Detection Range

To show the effect that evaporation duct height differences have on radar propagation properties, detection range predictions were computed for the ship data and the 3-km and 9-km COAMPS® data. This was done by inputing M profile predictions for the three data sources computed from the NPS evaporation duct model into APM (not as part of AREPS) which then computed propagation loss versus range curves for 6- and 100-ft height levels. A detection range was then estimated by finding the maximum range to the 140-dB propagation loss detection threshold value. Figure 34 shows an example from APM of a propagation loss versus range diagram. The lack of attenuation out to 100 NM suggested we use shorter ranges in our AREPS calculations.

The scatter plot of estimated detection range (Fig. 35) is similar to the evaporation duct height plot of Fig. 33. The detection range plot also shows the 3-km COAMPS® predicted values did not produce significant improvements over the 9-km COAMPS® values. The RMS errors for calculated detection range using the 9-km COAMPS® forecast values are lower than the 3-km calculated values at the 6-, 15- and 21-hr forecast times. All but the 12-hr forecasts show that the use of the MCSST sea temperature is better than the IR probe on the R/S Acoustic Explorer. The 12-hr forecasts using the 3-km COAMPS® with either SST are better than the 9-km COAMPS® forecasts.

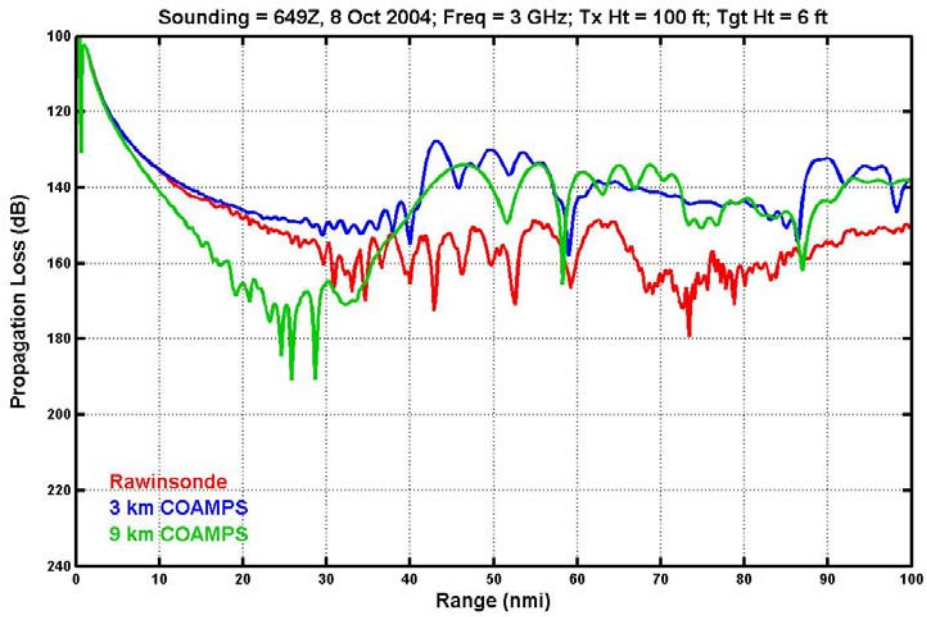

Fig. 34. Propagation Loss versus range for 6-ft target height at 3 GHz using APM with rawinsonde and COAMPS® modified refractivity profiles.

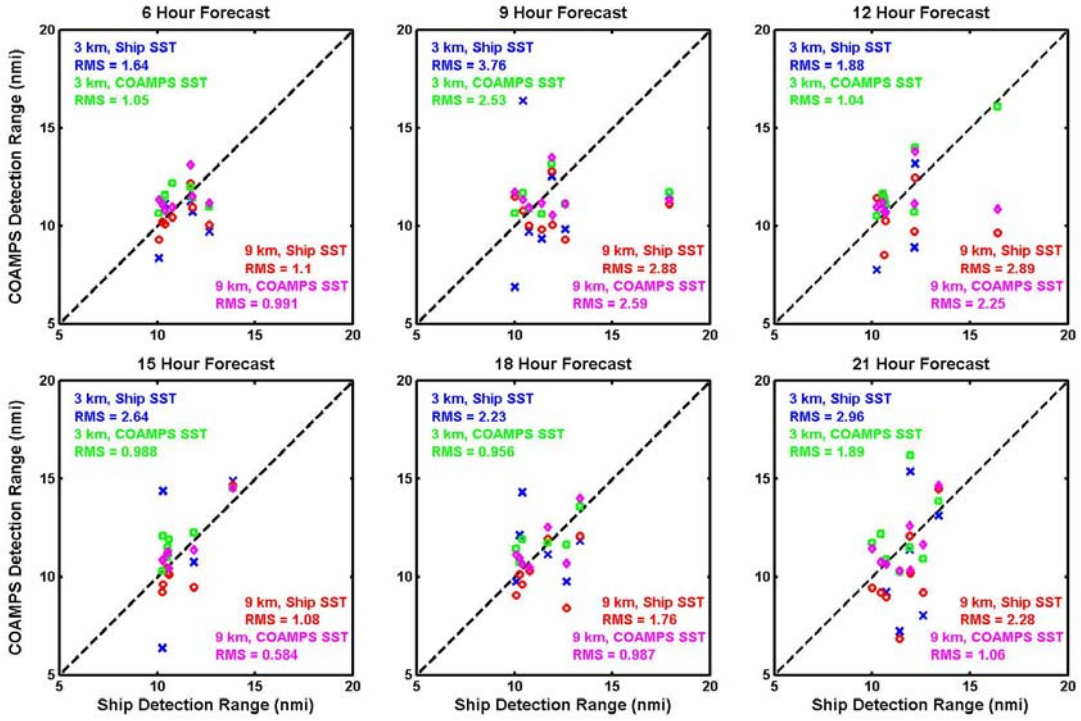

Fig. 35. Scatter plots of COAMPS® calculated detection ranges every three hours from the 6- to 21-hr forecasts.

IV. CONCLUSIONS AND RECOMMENDATIONS

A. DISCUSSION

This study examined the value of using COAMPS® data as input to propagation models and the potential improvement that might be derived by increasing the model's horizontal resolution. The evaluation was based on comparing *in-situ* meteorological observations and propagation-related parameters, computed from these observations, with the corresponding values predicted by two COAMPS® runs made with different horizontal resolutions. The results of these comparisons suggest that higher horizontal resolution does not necessarily improve the fidelity of COAMPS® in predicting all the input parameters required to run EM propagation models. Specifically, pressure and temperature forecasts were not improved with use of the higher resolution. There was also no improvement in relative humidity forecasts. Statistics based on the difference between the observed and COAMPS®-predicted M values and the heights of significant M values also showed no real improvement from the 9-km to 3-km COAMPS® resolutions. With respect to M values only, three of the first eleven sigma levels for the 9-km COAMPS® forecasts had lower RMS differences than the 3-km COAMPS® forecasts. Connecting these differences to height differences leads to gradient differences in M, which are the most important for analyzing variation in EM propagation.

The rawinsonde-observed and COAMPS®-predicted M profiles were compared to determine differences in the heights and strengths of trapping layers and their associated ducts. The 9-km COAMPS® forecasts were better with respect to the position of trapping layer base height than the 3-km COAMPS® forecasts (RMS errors of 162 versus 215 m). The 3-km COAMPS® runs did show a small improvement in detecting the overall duct heights, but the RMS errors for duct strength were nearly identical. Rawinsonde M profiles showing elevated ducts were not predicted well by either resolution of COAMPS®, but both did manage to correctly predict all six surface-based ducts on the 8th of October. However, surface-based ducts were predicted by both the 3- and 9-km COAMPS® profiles 12 times in cases when the concurrent rawinsonde profile showed that only an elevated duct was actually present. In summary, COAMPS® correctly predicted the actual type of duct (elevated, surface-based or none) observed in the

corresponding rawinsonde only eight out of 21 times at 9-km resolution and nine out of 21 times for the 3-km resolution.

The comparisons were extended to impacts on predicted detection ranges. Comparisons of AREPS predicted detection range did show a large improvement from the 9-km to 3-km runs. Looking at the same heights and propagation loss threshold values for both resolutions, the 9-km COAMPS® forecasts had a large number of positive and negative differences with a significant portion of those being over 13 NM. Most of the 3-km range variances were less than five NM, with only two of the 23 variances greater than 15 NM. The 3-km RMS difference in predicted detection range was smaller at 3.74 NM compared to the 9-km COAMPS® RMS difference of 15.02 NM. This analysis only examined those predicted detection ranges that were less than 50 NM. In a large number of cases, the detection range exceeded 50 NM and was therefore not included in the analysis.

Comparisons were also made between evaporation duct height and associated detection range estimates at a height of 6 feet based on input from the *in-situ* ship measurements and the lowest COAMPS® sigma level predictions. The evaporation duct height calculations based on using the COAMPS® air predictions and MCSST sea surface temperatures outperformed the use of COAMPS® with the ship sea temperature in every case examined for both 3- and 9-km resolutions. Although there were instances when the NPS bulk model did not calculate an evaporation duct height (i.e. greater than 50 m), both COAMPS® data combinations showed surprisingly good agreement with values calculated from the ship's sensor system. When using COAMPS® air data together with the MCSST values, the 9-km COAMPS® outperformed the 3-km COAMPS® in predicting evaporation duct height in half of the six forecast times examined. Not surprisingly, the comparison results for predicted detection range exactly mirrored those for the evaporation duct height in that whichever COAMPS® resolution performed best in predicting evaporation duct height also performed best in predicting the detection range. Each resolution had the smaller RMS error in half of the six forecast times examined. Therefore, although the 3-km COAMPS® multi-level profile data did better within AREPS for predicting propagation loss detection ranges at a height of 100 feet, it did not do significantly better when the lowest sigma level data only were used to forecast air

temperature, relative humidity, the evaporation duct height and its associated detection range at 6 feet. These results could be interpreted with respect to those of Dockery and Goldhirsh (1994) who found that 6-m vertical resolution and 17-km horizontal resolution were required for 5-dB propagation loss agreement between measurements and calculations.

B. FUTURE RESEARCH

One model property that appears to require more study is the optimum vertical resolution for the COAMPS® data. In the present study, both the 9-km and 3-km forecasts had the same 30 sigma levels. As with most research involving the MABL, it is recommended that more sigma levels are added in COAMPS® near the surface. This should help better resolve structures such as temperature inversions and trapping layers. As this study indicates, the model's horizontal resolution may not need to be as high as 3-km. FNMOC personnel recently examined 5-km COAMPS® data in conjunction with an exercise conducted off the coast of Florida with Submarine Development Squadron 12. It would be interesting to see how the 5-km runs compare with the 3-km resolution as well as the operational 9-km resolution.

The use of observed sea surface temperatures with COAMPS® air temperature forecasts as inputs to the NPS bulk model also requires further investigation. The lack of COAMPS® SST fields necessitated the use of observations in the calculations of EDH and detection ranges. This study shows a need for development in the field of data fusion. Perhaps the best forecasts in the future regarding EM propagation will come from a mixture of data sources incorporated into propagation models. Measured radar losses should be analyzed with predicted losses calculated using combinations of COAMPS® air values and different SST values from models like the Navy Operational Global Atmospheric Prediction System (NOGAPS), the Modular Ocean Data Assimilation System (MODAS) or the Navy Coastal Ocean Model (NCOM).

A parallel study should also be conducted by computer systems researchers. Since the time to process different resolutions of COAMPS® forecasts can be quantified, along with other factors such as cost of hardware and physical setup space, DOD computer programmers and engineers would be interested in evaluating the efficiency of these parameters at separate locations such as NAWC San Diego and FNMOC in Monterey,

Ca. U.S. Air Force computer and meteorological personnel could conduct a similar study of the MM5 model as well.

APPENDIX A: PREDICTED AND MEASURED M PROFILES

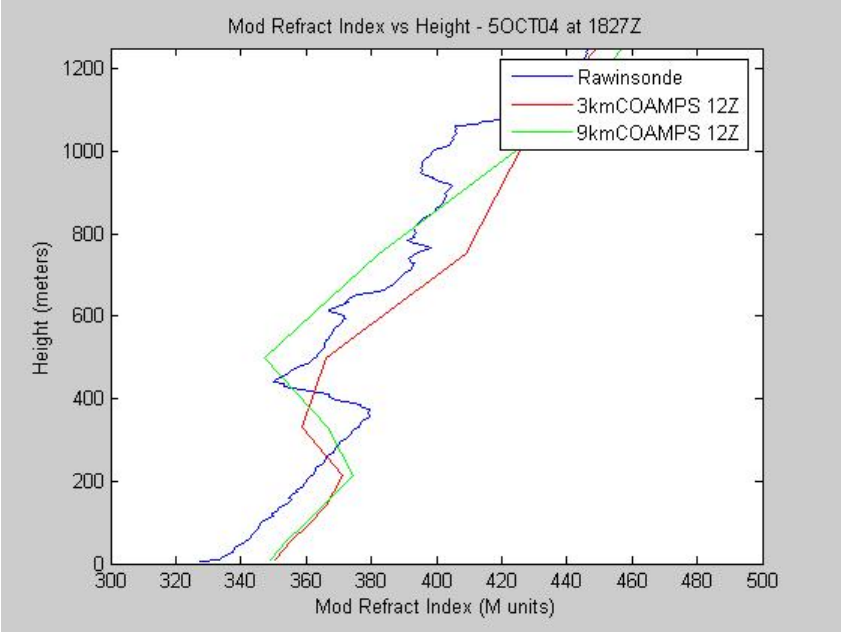

Fig. 34. M vs. height (in meters) for COAMPS 9km and 3km interpolations and October 5th 1827 UTC rawinsonde.

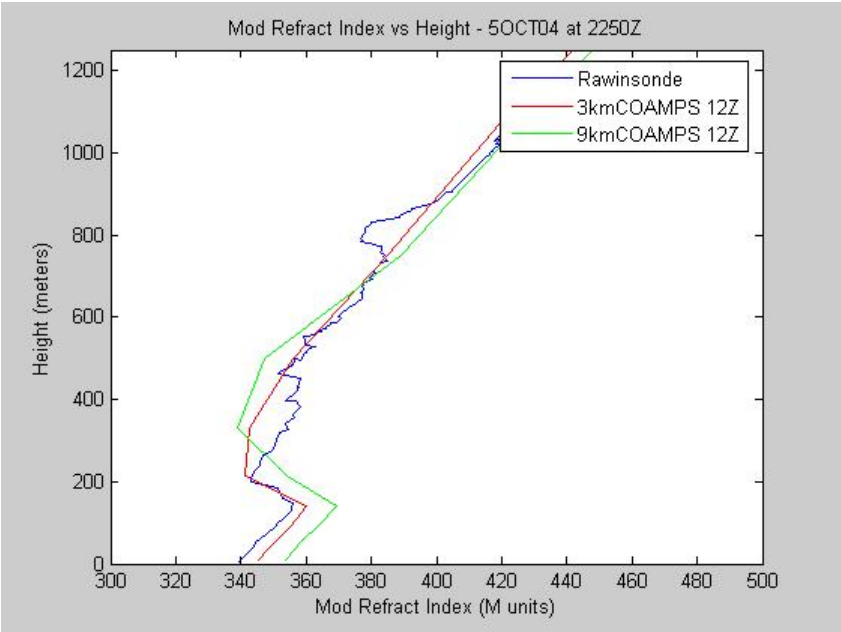

Fig. 35. M vs. height (in meters) for COAMPS 9km and 3km interpolations and October 5th 2250 UTC rawinsonde.

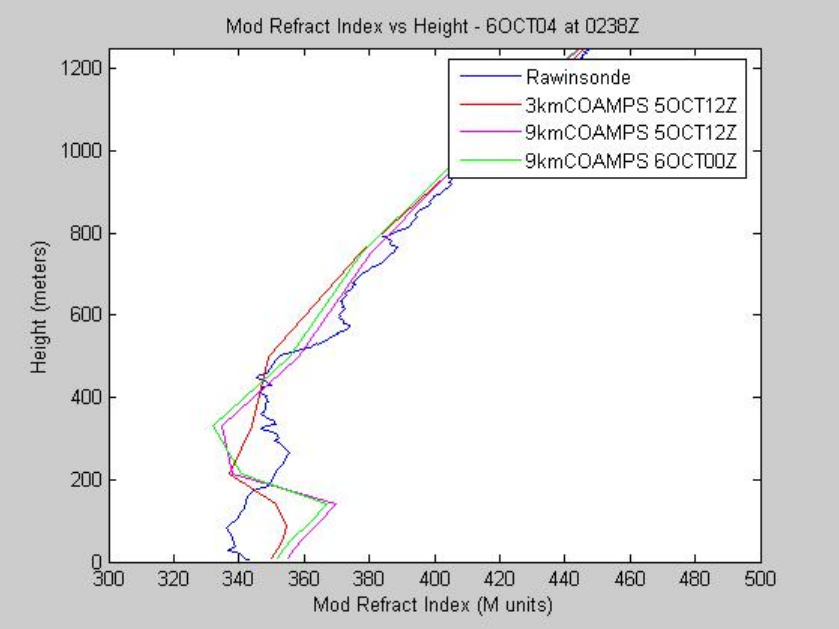

Fig. 36. M vs. height (in meters) for COAMPS 9km and 3km interpolations and October 6th 0238 UTC rawinsonde.

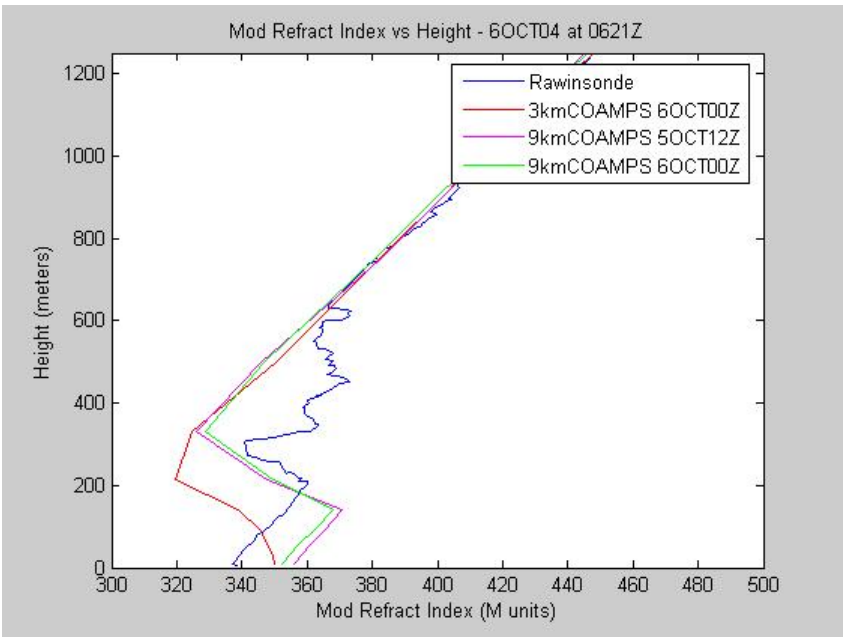

Fig. 37. M vs. height (in meters) for COAMPS 9km and 3km interpolations and October 6th 0621 UTC rawinsonde.

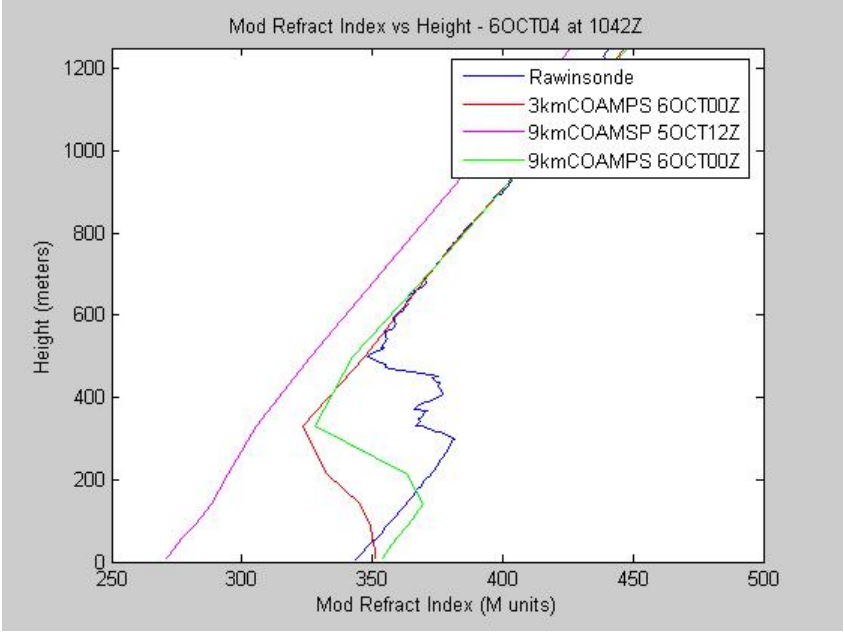

Fig. 38. M vs. height (in meters) for COAMPS 9km and 3km interpolations and October 6th 1042 UTC rawinsonde.

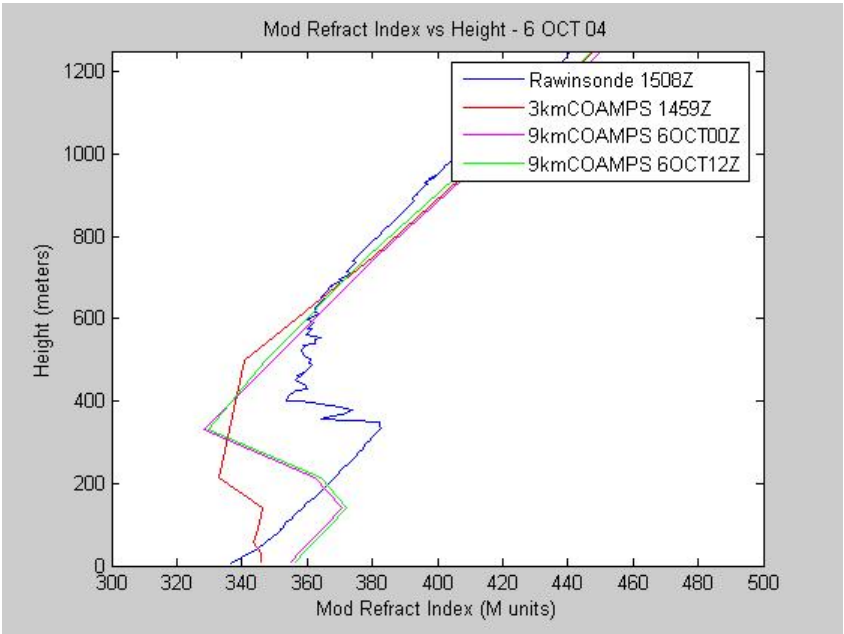

Fig. 39. M vs. height (in meters) for COAMPS 9km and 3km interpolations and October 6th 1508 UTC rawinsonde.

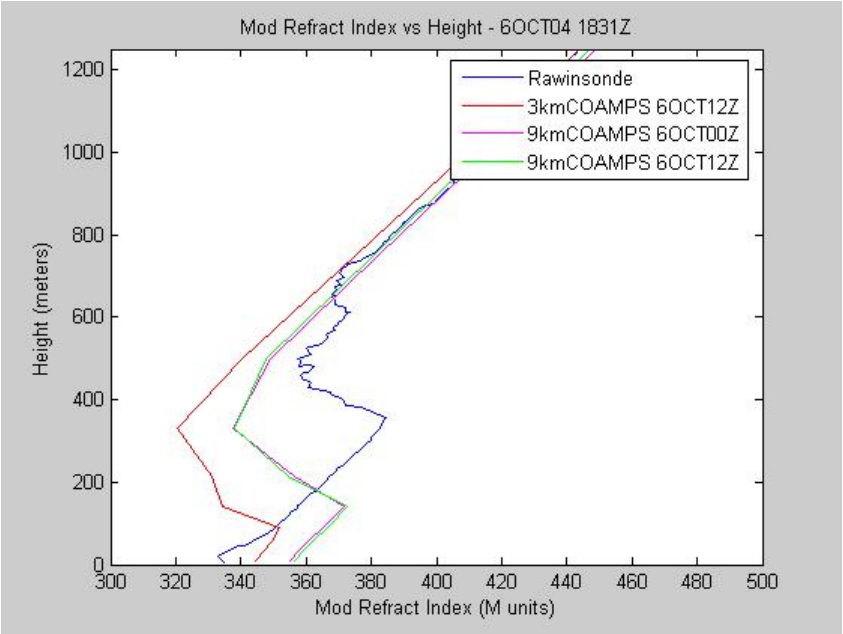

Fig. 40. M vs. height (in meters) for COAMPS 9km and 3km interpolations and October 6th 1831 UTC rawinsonde.

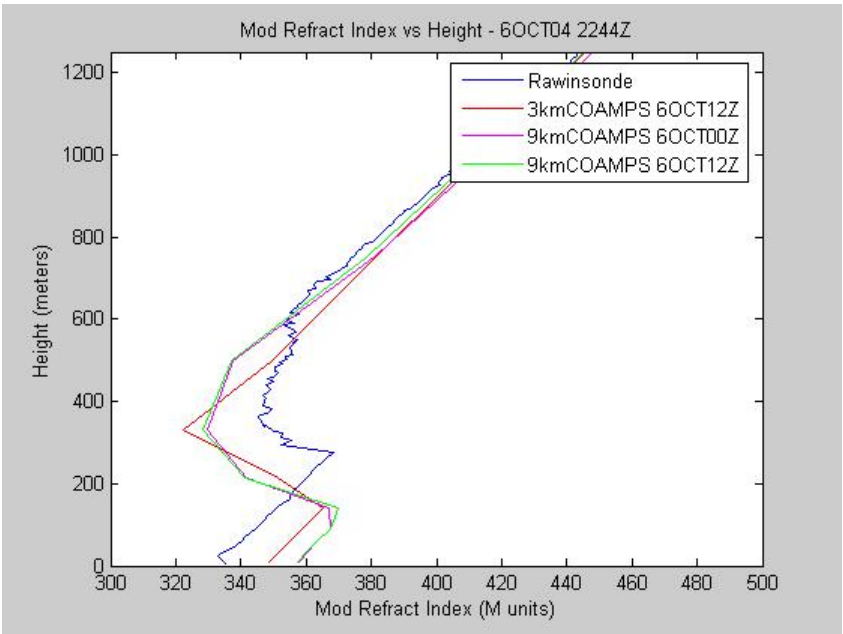

Fig. 41. M vs. height (in meters) for COAMPS 9km and 3km interpolations and October 6th 2244 UTC rawinsonde.

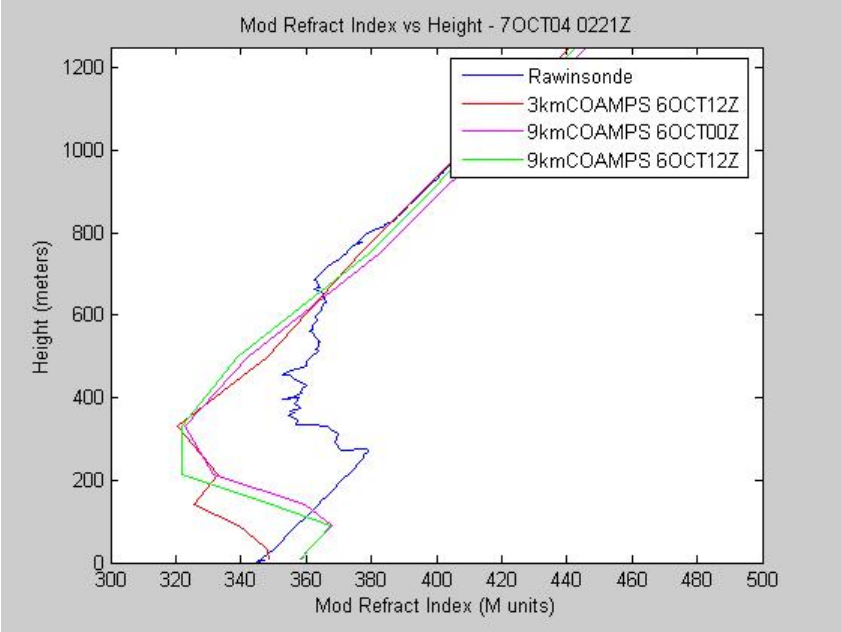

Fig. 42. M vs. height (in meters) for COAMPS 9km and 3km interpolations and October 7th 0221 UTC rawinsonde.

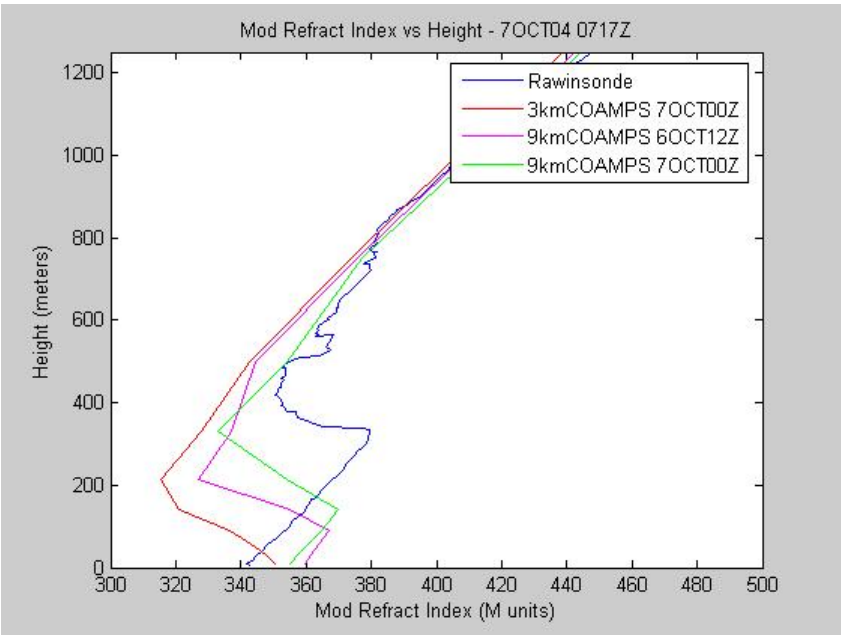

Fig. 43. M vs. height (in meters) for COAMPS 9km and 3km interpolations and October 7th 0717 UTC rawinsonde.

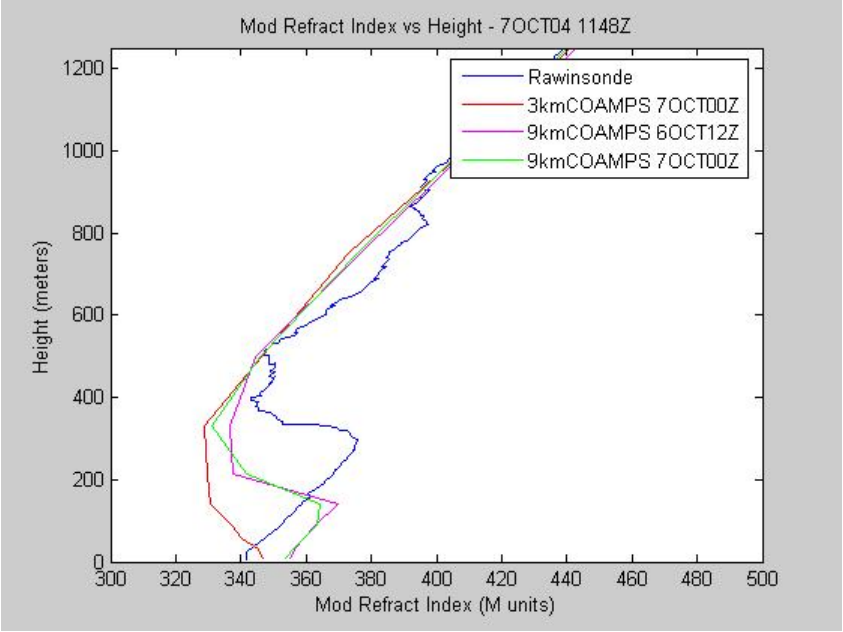

Fig. 44. M vs. height (in meters) for COAMPS 9km and 3km interpolations and October 7th 1148 UTC rawinsonde.

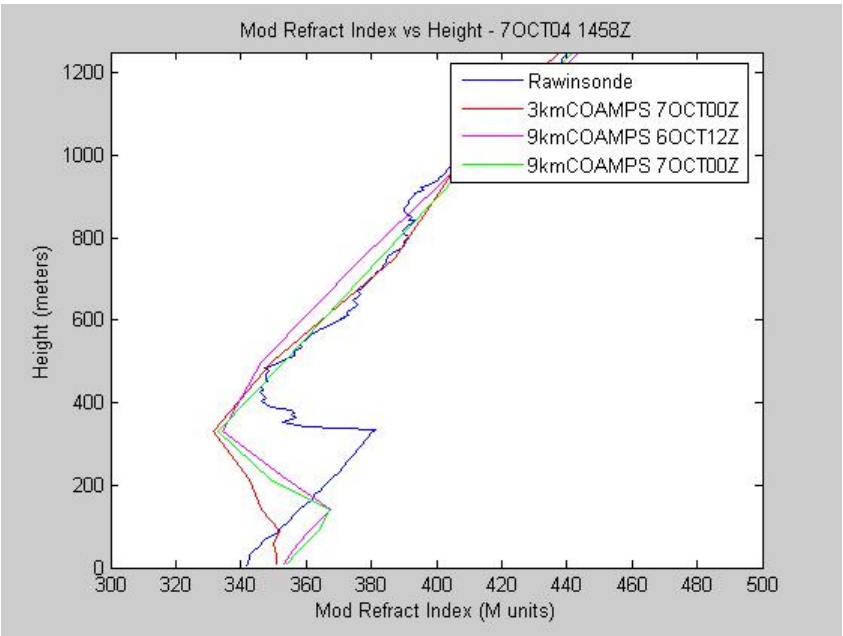

Fig. 45. M vs. height (in meters) for COAMPS 9km and 3km interpolations and October 7th 1458 UTC rawinsonde.

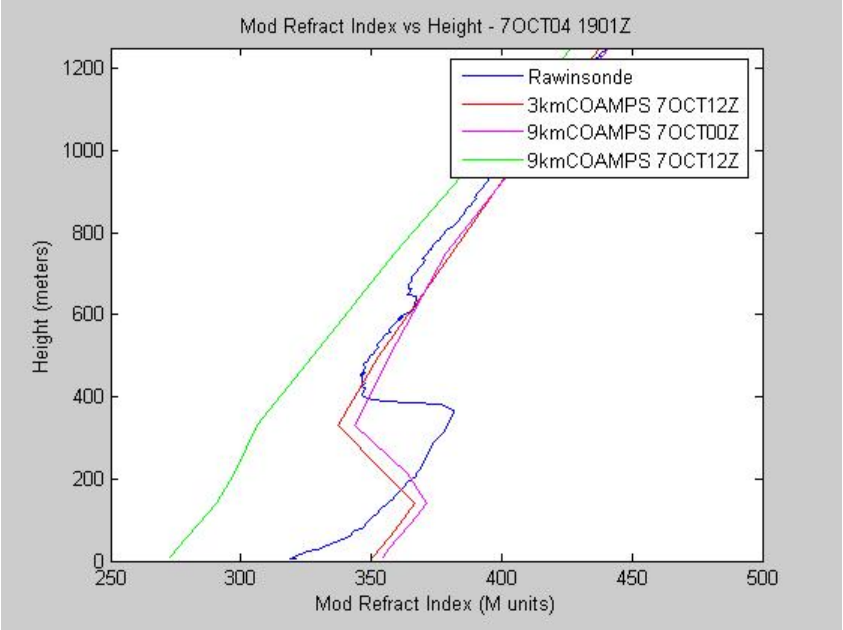

Fig. 46. M vs. height (in meters) for COAMPS 9km and 3km interpolations and October 7th 1901 UTC rawinsonde.

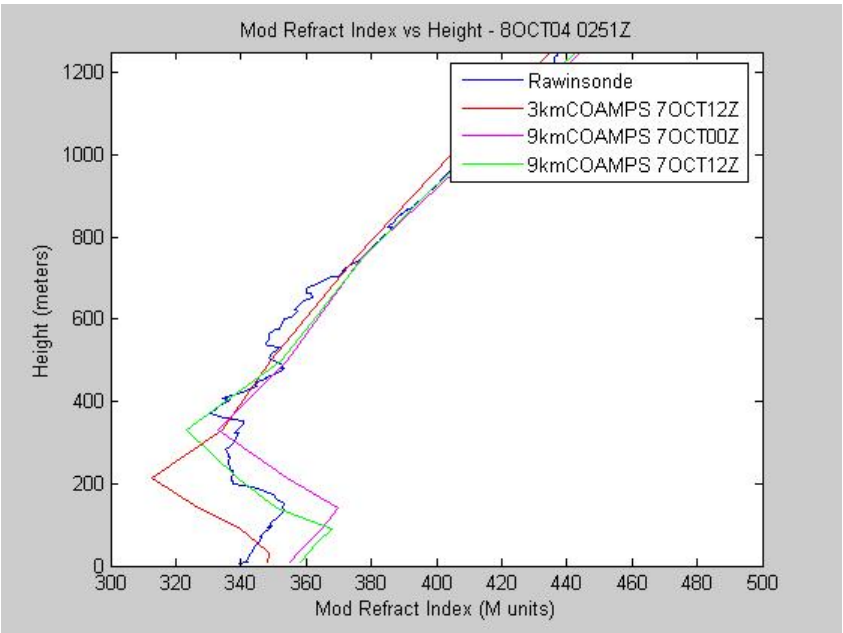

Fig. 47. M vs. height (in meters) for COAMPS 9km and 3km interpolations and October 8th 0251 UTC rawinsonde.

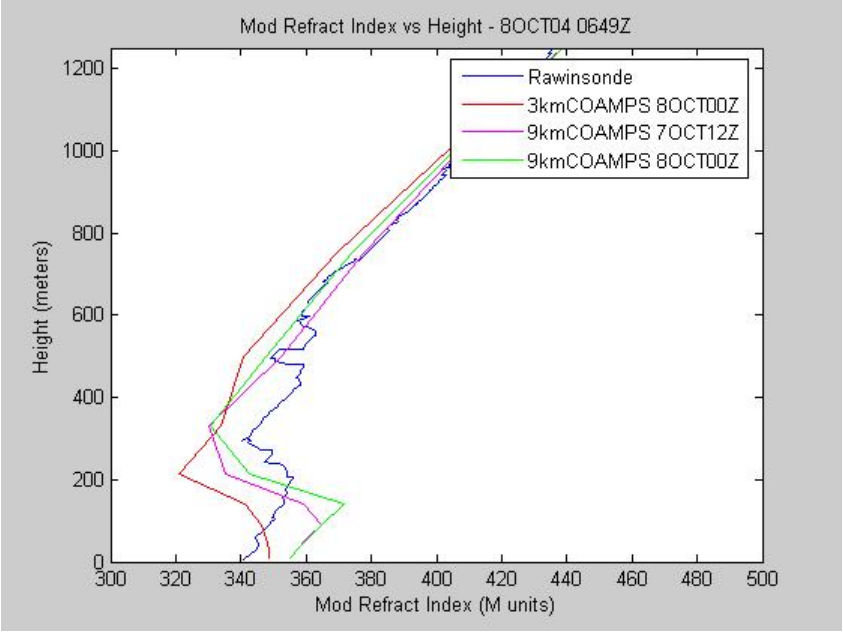

Fig. 48. M vs. height (in meters) for COAMPS 9km and 3km interpolations and October 8th 0649 UTC rawinsonde.

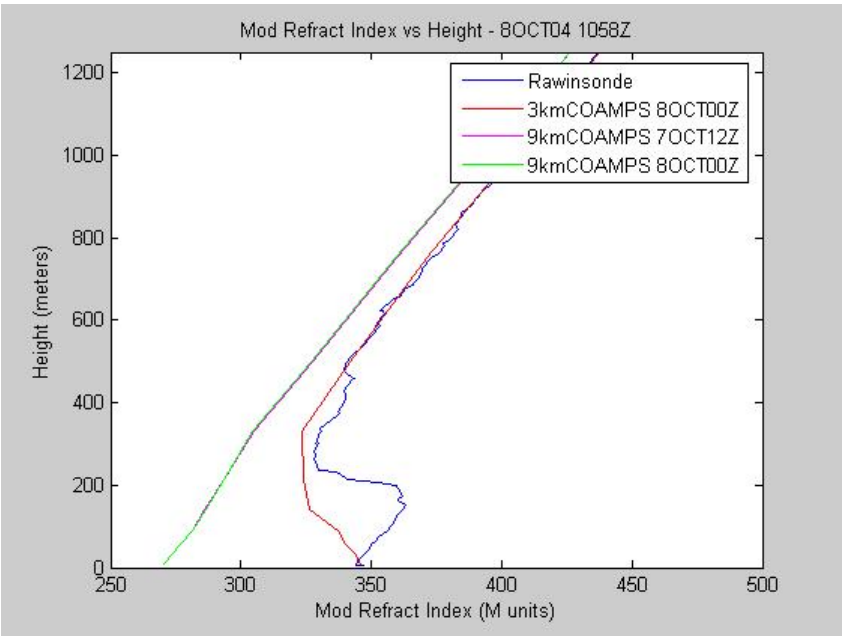

Fig. 49. M vs. height (in meters) for COAMPS 9km and 3km interpolations and October 8th 1058 UTC rawinsonde.

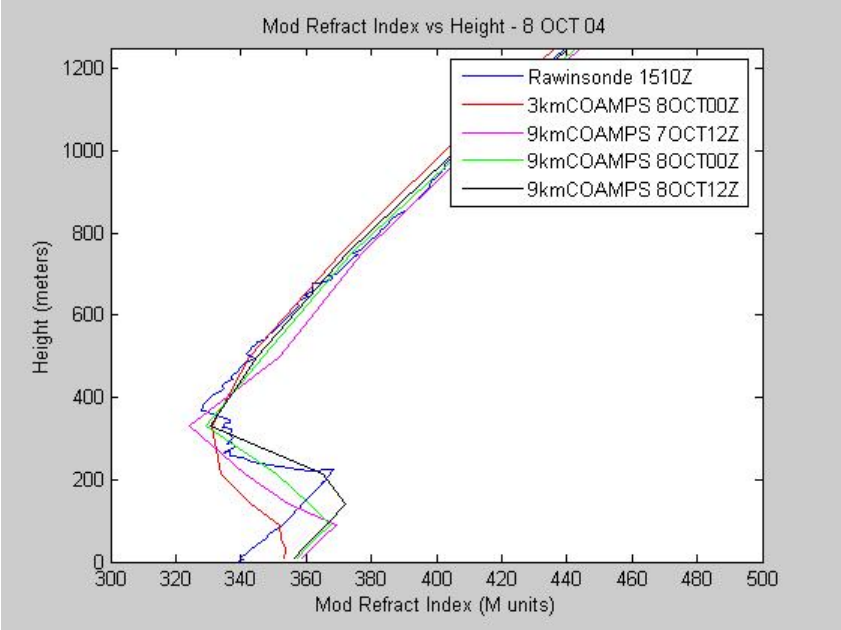

Fig. 50. M vs. height (in meters) for COAMPS 9km and 3km interpolations and October 8th 1510 UTC rawinsonde.

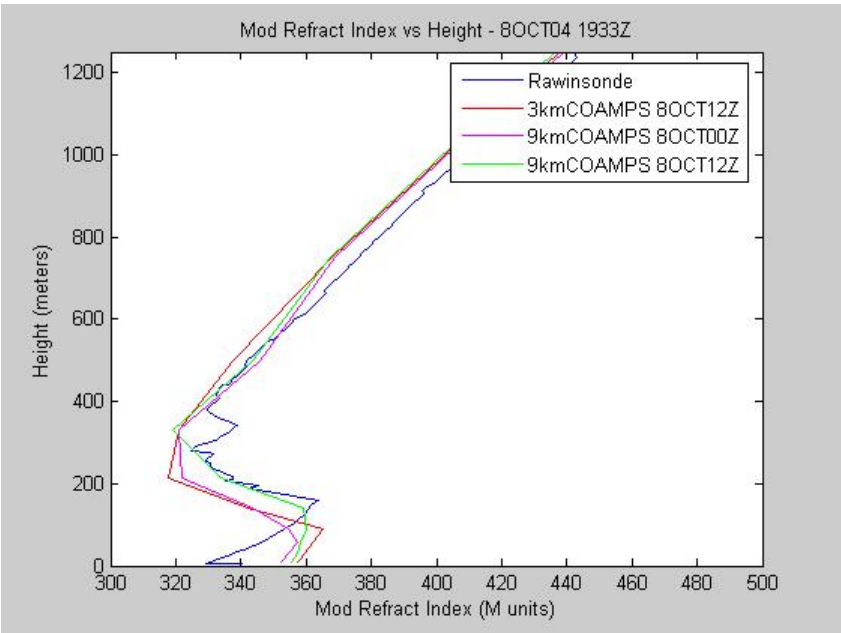

Fig. 51. M vs. height (in meters) for COAMPS 9km and 3km interpolations and October 8th 1933 UTC rawinsonde.

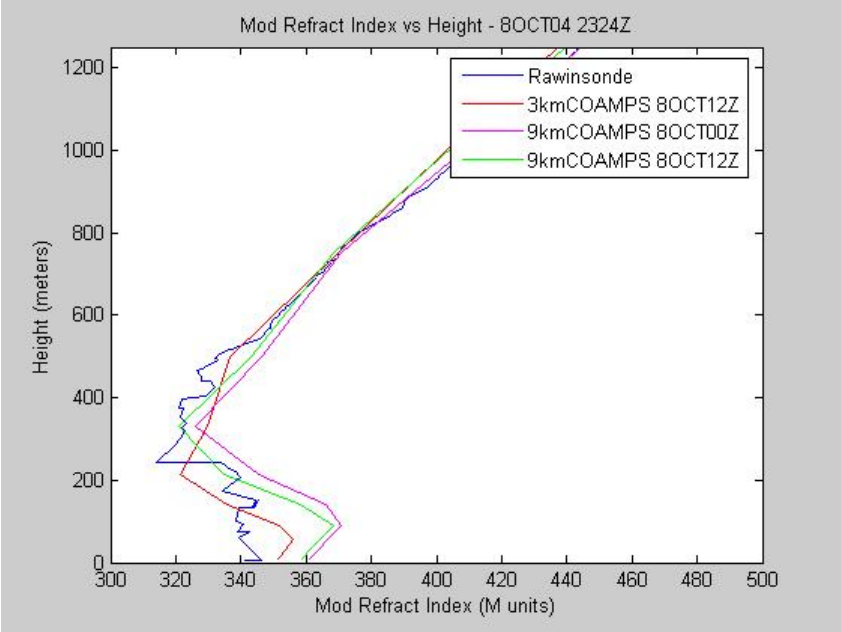

Fig. 52. M vs. height (in meters) for COAMPS 9km and 3km interpolations and October 8th 2324 UTC rawinsonde.

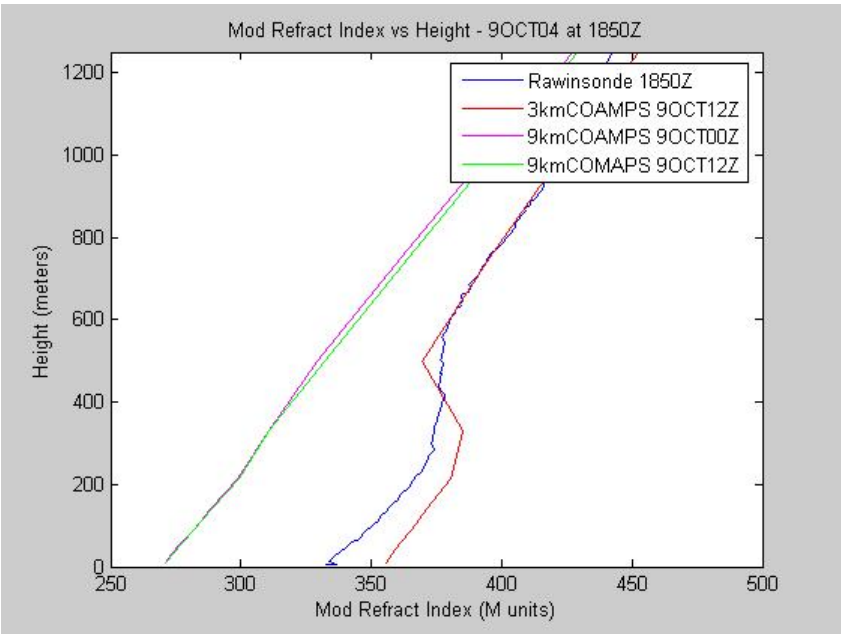

Fig. 53. M vs. height (in meters) for COAMPS 9km and 3km interpolations and October 9th 1850 UTC rawinsonde.

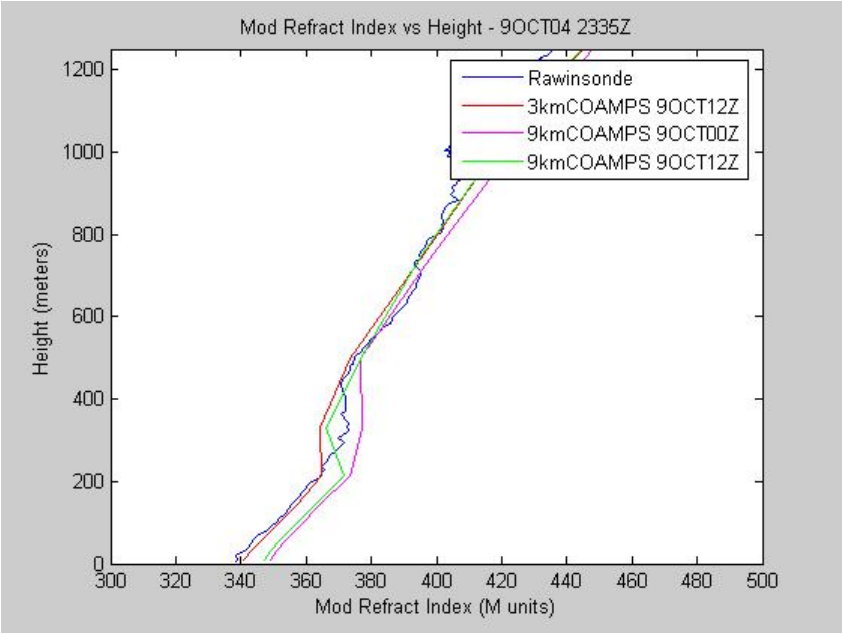

Fig. 54. M vs. height (in meters) for COAMPS 9km and 3km interpolations and October 9th 2335 UTC rawinsonde.

THIS PAGE INTENTIONALLY LEFT BLANK

LIST OF REFERENCES

Atkinson, B. W., J.-G. Li, and R. S. Plant, 2001: Numerical Modeling of the Propagation Environment in the Atmospheric Boundary Layer Over the Persian Gulf. *J. Appl. Meteor.*, 40, 586-603.

Atmospheric Instrumentation Research, Inc., 1992: Intellisensor Digital Barometer/ Altimeter User Manual.

Andreas, E. L., 1987: On the Kolmogorov Constants for the Temperature-Humidity Cospectrum and the Refractive Index Spectrum. *J. Atmos. Sci.*, 44, 2399-2406.

Babin, S. M. and G. D. Dockery, 2001: LKB-Based Evaporation Duct Model Comparison with Buoy Data. *J. Appl. Meteor.*, 41, 434-446.

Babin, S. M., G. S. Young, and J. A. Carton, 1997: A New Model of the Oceanic Evaporation Duct. *J. Appl. Meteor.*, 36, 193-203.

Barrios, Amalia E., 2003: Considerations in the Development of the Advanced Propagation Model (APM) for U.S. Navy Applications. *Proc. IEEE Conf. on Radar, 6 pp*.

Bean, B. R., and E. J. Dutton, 1968: *Radio Meteorology*. Dover Publications, New York, 435 pp.

Bradley, E. F., C. W. Fairall, J. E. Hare, and A. A. Grachev, 2000: An old and improved bulk algorithm for air-sea fluxes: COARE 2.6A. Preprints, *14th Symp. on Boundary Layers and Turbulence*, Aspen, CO, Amer. Meteor. Soc., 3 pp.

Burk, S. D., W. T. Thompson, J. Cook and G. G. Love, 1995: Mesoscale Modeling of Refractive Conditions During the VOCAR Experiment. *AGARD Lecture Series, Propagation Assessment in Coastal Environments*, North Atlantic Treaty Organization, 402-404.

Campbell Scientific, Inc., 1997: CS105 Barometric Pressure Sensor.

Campbell Scientific, Inc., 2002: IRTS-P Precision Infrared Temperature Sensor.

Climatronics Corporation, February 2002.

Doggett, M. K., 1997: An Atmospheric Sensitivity and Validation Study of the Variable Terrain Radio Parabolic Equation Model (VTRPE). Master's thesis, Air Force Institute of Technology, 76 pp.

Driggers, R.G., P. Cox and T. Edwards, 1999: *Introduction to Infrared and Electro-Optical Systems*. Artech House, Inc., 407 pp.

Davidson, K. L., G. E. Schacher, C. W. Fairall and A. K. Goroch, 1981: Verification of the Bulk Method for Calculating Overwater Optical Turbulence. *Appl. Opt.*, 20, no. 17, 2919-2923.

Dockery, G. D. and J. Goldhirsh, 1995: Atmospheric Data Resolution Requirements for Propagation Assessment: Case Studies of Range-Dependent Coastal Environments. *AGARD Conf. Proc. 567*, 12 pp.

Fairall, C. W., E. F. Bradley, D. P. Rogers, J. B. Edson and G. S. Young, 1996: Bulk parameterization of air-sea fluxes for Tropical Ocean-Global Atmosphere Coupled-Ocean Atmosphere Response Experiment. *J. Geophys. Res.*, 101, 3747-3764.

Frederickson, P. A., K. L. Davidson, C. R. Zeisse, and C. S. Bendall, 2000: Estimating the Refractive Index Structure Parameter (C_n^2) Over the Ocean Using Bulk Methods. *J. Appl. Meteor.*, 39, 1770-1783.

Garmin International, Inc., January 2002: GPS 16/17 Series Technical Specifications.

Hermann, J. A., A. S. Kulessa, C. Lucas, R. A. Vincent, J. M. Hacker, and C. M. Ewenz, 2002: Impact of Elevated Atmospheric Structures Upon Radio-Refractivity and Propagation. *Conf. Proc. Workshop on the Applications of Radio Science: Commission F*, 4 pp.

Hitney, H. V., Evaporation-Duct Assessment from Meteorological Buoys. *Radio Sci.*, 37, no. 4, 20 pp.

Hitney, H. V., Hybrid Ray Optics and Parabolic Equation Methods for Radar Propagation Modeling. Naval Command, Control and Ocean Surveillance Center Report, 58-61.

Hodur, R. M., 1997: The Naval Research Laboratory's Coupled Ocean/Atmosphere Mesoscale Prediction System (COAMPS). *Mon. Wea. Rev.*, 125, 1414-1430.

Chen, S. and Co-authors, 2003: COAMPS Version 3 Model Description. Naval Research Laboratory, Marine Meteorology Division.

Naval Research Laboratory, 2003: *Builder* 3.0 Manual and Tutorial (Pre-release 3). [Available online at https://*Builder*.nrl.navy.mil.]

Remcom, Inc., July 2003: A Basic Guide for Electromagnetic Wave Propagation Models. [Available online at https://*Builder*.nrl.navy.mil.]

ROTRONIC Instrument Corp., 2003: MP 100H/MP 400H Humidity Temperature Probe.

Smith, S. D., 1988: Coefficients for Sea Surface Wind Stress, Heat Flux, and Wind Profiles as a Function of Wind Speed and Temperature. *J. Geophys. Res.*, 93, 15467-15472.

Tsuda, T., M. Miyamoto, and J.-I. Furumoto, 2001: Estimation of a Humidity Profile Using Turbulence Echo Characteristics. *J. Atmos. Oceanic Technol.*, 18, 1214-1221.

Wash, C. H., M. S. Jordan and J. Cook, 1998: Evaluation of COAMPS Mesoscale Modeling in the Persian Gulf Region. *Proc. of BACIMO*, 8 pp.

Wetzel, M. A., S. K. Chai and D. R. Koracin, 2004: Final Report to the Office of Naval Research for Project Entitled "Multispectral Remote Sensing and COAMPS Model Analysis Methods for Marine Cloud Structure, Entrainment Processes and Refractivity Effects", 17 pp.

Willoughby, A. A., T. O. Aro, and I. E. Owolabi, 2002: Seasonal Variations of Radio Refractivity Gradients in Nigeria. *J. Atmos. Terr. Phys.*, 64, 417-425.

INITIAL DISTRIBUTION LIST

1. Defense Technical Information Center
   Ft. Belvoir, VA

2. Dudley Knox Library
   Naval Postgraduate School
   Monterey, CA

3. The Oceanographer of the Navy
   U.S. Naval Observatory
   Washington, D.C.

4. Prof. Kenneth L. Davidson, MR/DS
   Dept. of Meteorology
   Naval Postgraduate School
   Monterey, CA

5. Lee Eddington
   Geophysics Branch
   NAWC/CWPNS
   Point Mugu, CA

6. Dr. R. Ferek, Code 322 MM
   Office of Naval Research
   Arlington, VA

7. Dr. Shelley Gallup
   Dept. of Information Sciences
   Naval Postgraduate School
   Monterey, CA

8. Dr. A. Goroch
   Naval Research Laboratory
   Monterey, CA

9. Tracy Hack
   Naval Research Laboratory
   Monterey, CA

10. Wayne Patterson
    SPAWARSYSCEN-SD, 2858
    San Diego, CA

11. Thomas Piwowar, PMW 180
PEO C4I & Space
San Diego, CA

12. CAPT Vic Addison, CO
Fleet Numerical Meteorology and Oceanography Center
Monterey, CA